AERODYNAMICS OF UAV GROUND EFFECT INTERACTIONS

by

William P. Timms

A thesis submitted to the faculty of
The University of North Carolina at Charlotte
in partial fulfillment of the requirements
for the degree of Master of Science in
Mechanical Engineering

Charlotte

2021

Approved by:

____

Dr. Mesbah Uddin

____

Dr. Artur Wolek

____

Dr. Jun Xu

ABSTRACT

WILLIAM P. TIMMS. Aerodynamics of UAV Ground Effect Interactions. (Under the direction of DR. MESBAH UDDIN)

With the advent of quadrotor unmanned aerial vehicles (UAV) becoming more prevalent for military and commercial applications, gaining a better understanding of their aerodynamic characteristics is critical. No matter the application, each operation begins and ends with vertical takeoff and landing (VTOL). Therefore, investigating the aerodynamic effects of ground proximity on thrust, wake, and vehicle stability is required to ensure safe operation. Based on previous use in published experimental studies, 0.240 m diameter rotor models with a rotation rate of 4860 RPM were used in the present work. A finite volume commercial Computational Fluid Dynamics (CFD) code STAR-CCM+ by Siemens was used to run three-dimensional implicit Unsteady Reynolds Averaged Navier-Stokes (URANS) simulations of a Da-Jiang Innovations (DJI) Phantom UAV utilizing dynamic meshing techniques for rotor motion and VTOL scenarios. Model validation was achieved by first simulating single and dual rotor cases to compare predictions of thrust and rotor-rotor interactions to published data. Following this, a full UAV was modeled in a hovering scenario far from solid boundaries to provide a baseline case. The single rotor simulation showed a 5.625% overshoot in thrust compared to an expected value of 3 N, and a 1.473% overshoot compared to a comparable published RANS simulation. At a minimum tip separation distance of $0.05D$, a drop in time-averaged thrust of 1.256% and 1.186% was found for the dual rotor and baseline UAV cases compared to an expected drop of ~2%. Upon successfully validating the CFD simulation framework, the baseline UAV simulation was repeated for seven scenarios, having the UAV hover at heights between 3.0 m and ground level with a step change of 0.5 m. These simulations were used to compare how ground effect can change thrust and alter the wake formation.

It was determined that ground effect was negligible beyond a height of 1.5 m for this UAV. Thus, the hovering cases beyond 1.5 m were omitted. Finally, a dynamic scenario was simulated having the UAV land from a height of 3.0 m, which was used to assess the stability of the UAV in VTOL by monitoring the pitching moment. Future work will be able to build from these simulations to create reduced order models and investigate more complex scenarios such as UAV-ground vehicle wake interactions.

DEDICATION

For my parents, Kenneth and Marina Timms, and my late grandmother, Maria Naska. None of this would have been possible without your support.

ACKNOWLEDGEMENTS

First, I would like to thank my advisor, Dr. Mesbah Uddin, for his encouragement and support throughout my entire time in graduate school. His constant feedback and direction has helped me focus my interests and develop my technical skills. I would also like to thank Dr. Artur Wolek and Dr. Jun Xu for providing valuable feedback for my proposal defense and agreeing to be members of my thesis committee. Next I would like to thank Dr. Jerry Dahlberg and Dr. Russell Keanini for aiding my admission process for the MSME program. I would also like to thank my colleague, Adit Misar, for all of his help and advice throughout this research project. Finally, I would like to thank Dr. Rodward Hewlin Jr. for igniting my passion for Fluid Dynamics in undergrad, and ultimately convincing me to go to graduate school in the first place.

TABLE OF CONTENTS

LIST OF TABLES

LIST OF FIGURES

CHAPTER 1: INTRODUCTION

Quadrotor unmanned aerial vehicles (UAV) have become significantly more popular for a wide variety of applications over the past decade. They are valuable for their small size and ability to perform vertical takeoff and landing (VTOL) operations. UAV have been looked at for commercial operations such as package delivery, where companies such as Amazon and Google, as well as other large e-commerce companies, have already begun development of UAV solutions as a method of cutting the cost of labor [1]. There have also been uses for agricultural UAV for spraying pesticides on crops without being limited by crop growth or other landscape related restrictions [2]. There are infrastructural uses for UAV as well such as for wind harvesting at higher altitudes [3], or even urban transportation like the NASA Quadrotor urban air taxi concept [4]. Outside of commercial uses, small UAV have proven useful for scientific discovery as well. A few examples of this are gathering samples of materials in difficult to reach locations such as algae in the center of a lake [5], or carrying small sensing payloads for airborne wind measurments [6], or even for taking long-dwell topographic imagery for low-cost nearshore measurements [7]. Finally, UAV have been used in military applications, such as real time surveillance [8] or all-terrain payload delivery and retrieval [9].

Regardless of the application, the beginning and end of any operation is VTOL. In these scenarios, ground effect has been shown to increase thrust at the expense of stability [10]. It has also been shown to cause the formation of large clouds of dust or snow that could lead to a lack of visibility for remote pilots and cause a crash [11]. For this reason, characterizing the UAV wake in ground effect is important. However, using experimental methods to determine these effects could become very expensive.

Multiple setups would be required for thrust measurements, wake characterization, and stability measurements, and a relatively large wind tunnel would also be required to allow for significant variations in hovering height. In contrast, Computational Fluid Dynamics (CFD) can easily be setup to do all of these simultaneously, and can quickly be tailored for further scenarios introducing more variables.

To quickly summarize, the goals of the present work are to build a CFD framework in STARCCM+ using a URANS methodology for a Da-Jiang Innovations (DJI) Phantom UAV by first validating a single and dual rotor case to ensure accuracy in predictions of thrust and rotor-rotor interactions. Following this, the full UAV can be modeled and general trends of the wake can be compared to similar UAV simulations to ensure accurate wake characterization. With the framework validated, several simulations can be run to examine how ground effect can affect thrust, wake formation, and UAV stability. The main contributions of this thesis are determining the magnitude of change in thrust due to ground effect for this UAV, the change in wake formation at several heights above the ground as well as the height in which ground effect is negligible, and how ground effect changes UAV stability via changes in pitching moment.

Before moving to the methodology used to investigate UAV ground effect, it is important to describe some terminology for rotorcraft. A helicopter, or in this case UAV, is said to be in ground effect when the rotors are less than a few rotor diameters above the ground. When at this height, the proximity of the ground alters aerodynamic characteristics of the rotors. As a rotor spins, the cross-sectional airfoil generates lift, which is often called a rotor's thrust. The air that is deflected downwards can be called the downwash, which characterizes the wake of the rotor. When describing parts of this wake, rather than using terms like inside, outside, right, or left, the terms retreating and advancing are used to reference the side of the rotor's blade being discussed. For simplification, a schematic describing what that means for a helicopter can be seen in Fig. 1.1 [12]. This shows that part of the blade moving forward against the incoming air is the advancing side, while the part of the blade moving backward with the incoming air is the retreating side. The same also applies to UAV.

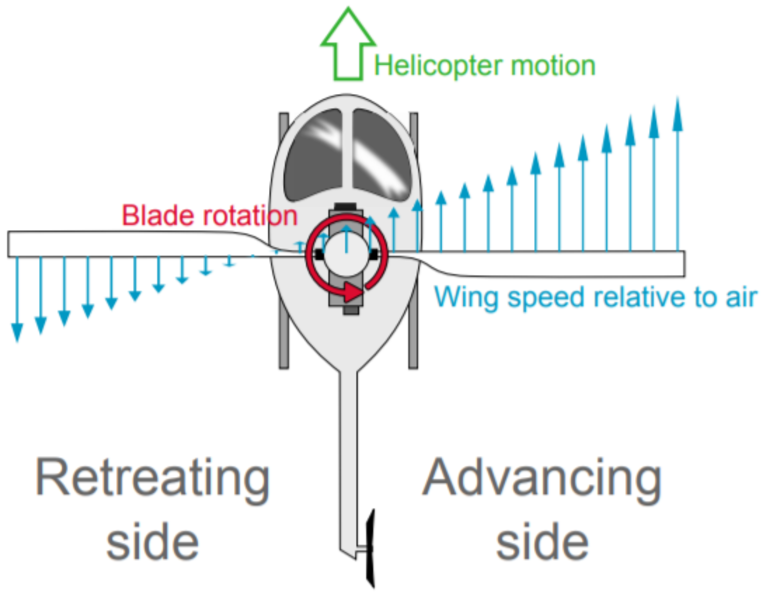

Figure 1.1: A schematic defining what advancing and retreating blades are [12].

Two important phenomena that are repeatedly discussed here are tip vortices and shear layers. Tip vortices are vortices that occur wherever a lift producing device, such as a wing or rotor blade, terminates in the air. The pressure differential between the high pressure on the bottom of the blade and low pressure on the top of the blade causes the flow to accelerate around the blade tip and generate a tip vortex [13]. A schematic describing this phenomena can be seen in Fig. 1.2a. Shear layers are described as a thin region of concentrated vorticity where the tangential velocity component varies greatly [14]. This phenomena occurs in rotors when the boundary layers from the upper and lower surfaces of the blade merge [15], and a simplified two-dimensional schematic of this can be seen in Fig. 1.2b.

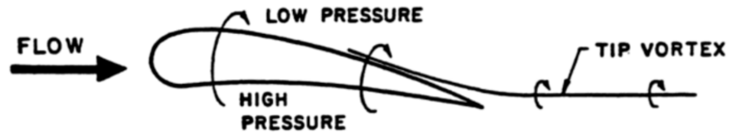

(a) Tip vortices

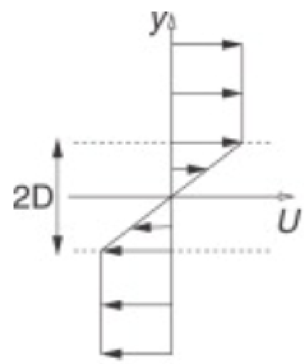

(b) Shear layers

Figure 1.2: A schematic describing (a) the generation of tip vortices [13] and (b) a 2D shear layer [14].

CHAPTER 2: METHODOLOGY

2.1 Governing Equations and Turbulence Models

A three-dimensional implicit Unsteady Reynolds-Averaged Navier-Stokes (URANS) Simulation was conducted for all following studies. The turbulence model chosen was the k-ω Shear Stress Transport (SST) with an ideal gas model. The k-ω SST model has been widely used in rotor investigations [2, 16, 17, 18, 19, 20, 21, 22]. In simulations where the Mach number is below 0.3, the effects of compressibility are negligible, and therefore allow for the use of the ideal gas model.

Two-equation models like the k-ω SST model include two extra transport equations, where in this case the transported variables are the turbulent kinetic energy, k, and the specific rate of dissipation, ω. The k-ω model is ideal for modeling the viscous sublayer and boundary layer in flows with moderate adverse pressure gradients [23] as it does not involve any damping functions, and therefore allows simple Dirichlet boundary conditions to be specified. However, this model has difficulty accurately predicting turbulence as it asymptotically approaches the wall [24]. In this case, the k-ϵ model functions better in the wake region as the k-ω model is sensitive to freestream values of ω [23]. This led to the definition of eddy viscosity being modified to account for the transport of the turbulent shear stress, which resulted in the k-ω SST model [24].

The RANS equations in Einstein notation are given in 2.1 and 2.2. Next is the equation for the Reynolds Stresses in 2.3, followed by the definition of Kronecker Delta, δ_{ij}. Going forward, ρ is the fluid density, k is the turbulent kinetic energy, ω is the specific rate of dissipation, μ is the dynamic viscosity, ν is the kinematic viscosity, and S is the invariant measure of the strain rate.

$$\frac{\partial U_i}{\partial x_i} = 0 \tag{2.1}$$

$$\frac{\partial U_i}{\partial t} + U_j \frac{\partial U_i}{\partial x_j} = -\frac{1}{\rho}\frac{\partial P}{\partial x_i} + \frac{\partial}{\partial x_j}(2\mu S_{ij} - \rho\overline{u_i' u_j'}) \tag{2.2}$$

$$\overline{u_i' u_j'} = \frac{2}{3}k\delta_{ij} - \nu_t \left(\frac{\partial U_i}{\partial x_j} + \frac{\partial U_j}{\partial x_i} \right) \tag{2.3}$$

$$\delta_{ij} = \begin{cases} 1 & \text{if } i = j \\ 0 & \text{if } i \neq j \end{cases}$$

The two extra transport equations specific to the SST model are then given in 2.4 and 2.5 [23].

$$\frac{\partial(\rho k)}{\partial t} + \frac{\partial(\rho U_i k)}{\partial x_i} = \tilde{P}_k - \beta^* \rho k \omega + \frac{\partial}{\partial x_i}\left[(\nu + \sigma_k \nu_t) \frac{\partial k}{\partial x_i} \right] \tag{2.4}$$

$$\frac{\partial(\rho \omega)}{\partial t} + \frac{\partial(\rho U_i \omega)}{\partial x_i} = \alpha \rho S^2 - \beta \rho \omega^2 + \frac{\partial}{\partial x_i}\left[(\nu + \sigma_\omega \nu_t) \frac{\partial \omega}{\partial x_i} \right] + 2(1 - F_1)\rho\sigma_{\omega_2}\frac{1}{\omega}\frac{\partial k}{\partial x_i}\frac{\partial \omega}{\partial x_i} \tag{2.5}$$

2.6 and 2.7 are the blending functions that allow the SST model to transition from k-ω to k-ϵ depending on the distance from the wall (y), which is determined with Equation 2.5 [23].

$$F_1 = \tanh\left\{ \left\{ \min\left[\max\left(\frac{\sqrt{k}}{\beta^* \omega y}, \frac{500\nu}{y^2 \omega} \right), \frac{4\rho\sigma_{\omega_2} k}{CD_{k\omega}\, y^2} \right] \right\}^4 \right\} \tag{2.6}$$

$$F_2 = \tanh\left[\left[\max\left(\frac{2\sqrt{k}}{\beta^* \omega y}, \frac{500\nu}{y^2 \omega} \right) \right]^2 \right] \tag{2.7}$$

$$CD_{k\omega} = \min\left(2\rho\sigma_{\omega 2}\frac{1}{\omega}\frac{\partial k}{\partial x_i}\frac{\partial \omega}{\partial x_i}, 10^{-10}\right) \tag{2.8}$$

The turbulent eddy viscosity is given in 2.9 [23].

$$\nu_t = \frac{\alpha_1 k}{\max(\alpha_1 \omega, SF_2)} \tag{2.9}$$

A production limiter used to reduce the turbulence build-up in stagnation zones is given in 2.10 [23].

$$P_k = \nu_t \frac{\partial U_i}{\partial x_j}\left(\frac{\partial U_i}{\partial x_j} + \frac{\partial U_j}{\partial x_i}\right) \rightarrow \tilde{P}_k = \min(P_k, 10 \cdot \beta^* \rho k \omega) \tag{2.10}$$

Finally, 2.11 computes constants by a blend of closure coefficients (σ_{k1}, σ_{k2}, $\sigma_{\omega 1}$, $\sigma_{\omega 2}$, α_1, α_2, β_1, β_2, and β^*) from the k-ω and k-ϵ models [23].

$$\alpha = \alpha_1 F + \alpha_2(1 - F) \tag{2.11}$$

$$\sigma_{k1} = 0.85, \sigma_{\omega 1} = 0.5, \alpha_1 = 5/9, \beta_1 = 3/40, \beta^* = 0.09$$

$$\sigma_{k2} = 1.0, \sigma_{\omega 2} = 0.856, \alpha_2 = 0.44, \beta_2 = 0.0828, \beta^* = 0.09$$

An important quantity in characterizing turbulence is the vorticity, which is the curl of the velocity vector, or the infinitesimal rotation of that vector. It is defined in 2.12, with the tensor notation defined in 2.13. This is followed by the definition Levi-Civita operator, ϵ_{ijk}, as a skew-symmetric tensor. This operator serves as the alternating tensor in the definition of ω_i [25].

$$\vec{\omega} = \nabla \times \vec{u} \tag{2.12}$$

$$\omega_i = \epsilon_{ijk}\frac{\partial u_k}{\partial u_j} \tag{2.13}$$

$$\epsilon_{ijk} = \begin{cases} 0 & \text{for repeating indices: } i = j,\ j = k, \text{ or } k = i \\ 1 & \text{for cyclic indices: (1,2,3), (2,3,1), or (3,1,2)} \\ -1 & \text{otherwise: (2,1,3), (1,3,2), or (3,2,1)} \end{cases}$$

Another important quantity for observing turbulent structures is the Q-criterion, which is based on the second invariant Q of the velocity gradient tensor [26]. Areas where Q $>$ 0 shows the existence of vortices, and the Q-criterion is defined in 2.14−2.16 where S is the rate of strain and Ω is the vorticity tensor [27].

$$Q = -\frac{1}{2}(S_{ij}S_{ij} - \Omega_{ij}\Omega_{ij}) \tag{2.14}$$

$$S_{ij} = \frac{1}{2}\left(\frac{\partial u_i}{\partial x_j} + \frac{\partial u_j}{\partial x_i}\right) \tag{2.15}$$

$$\Omega_{ij} = \frac{1}{2}\left(\frac{\partial u_i}{\partial x_j} - \frac{\partial u_j}{\partial x_i}\right) \tag{2.16}$$

2.2 Geometry and Domain

2.2.1 Geometry

The rotors selected for this study were the exact models used to additively manufacture the rotors for an experimental study of rotor-rotor interactions [15]. The model was available for download from the BYU Flow Lab [28]. Fig. 2.1 shows the top, side, and profile view for the rotor geometry used in the present work. The rotor has a diameter of 0.240 m, which will often be referenced as D. It also uses an E63 airfoil as the cross-sectional shape. The chord length at the tip is 0.011 m, and the chord lengths along the length of the blade were determined by an optimal chord length equation given in 2.17, where C_{tip} is the chord length at the tip and r is a non-dimensional radius that equals zero at the blade center and one at the tip. The twist angle from the tip to 30% the length of the blade changes from 10° to 20°. These rotors were reported to have similar performance to the DJI Phantom 2 rotors, providing a 3.0 N thrust at a rotation speed of 4860 RPM [15].

$$C_r = \frac{C_{tip}}{r} \tag{2.17}$$

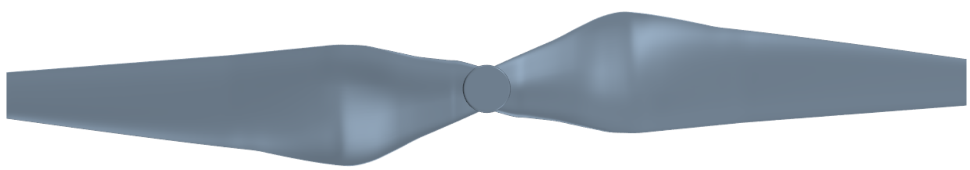

(a) Rotor top view

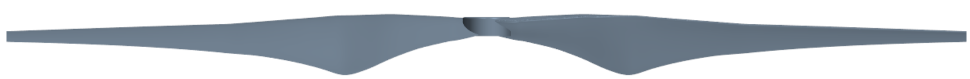

(b) Rotor side view

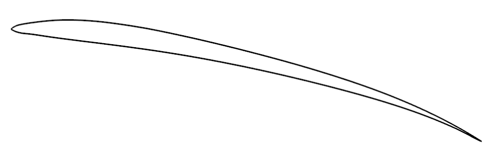

(c) E63 airfoil profile

Figure 2.1: Rotor model used in the present study shown in (a) top view, (b) side view, and (c) airfoil profile.

The UAV model used in the present work is the DJI Phantom 3. This model was chosen as it is a very popular UAV with models widely available for download. This specific model was acquired and cleaned in ANSA by a peer [29]. The initial rotors on the model were replaced with those discussed previously as it was valuable to use rotors with good experimental data for comparison. Fig. 2.2 shows the top and front views of the UAV model. The motors were removed for simplicity as the fine details would be difficult to mesh without added computational expense. However, the rotors remain at the height where they would be attached to the motors, where the distance between the rotor base and the landing gear of the UAV is approximately 0.2 m. The coordinate system is also denoted in these images, showing the x, y, and z to represent the stream-wise, span-wise, and ground-normal directions. The x, y, and z directions also correspond to the i, j, and k components.

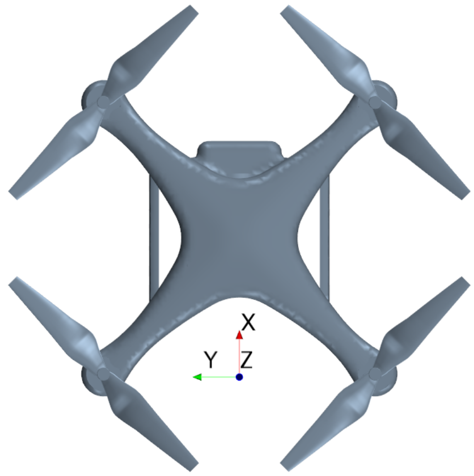

(a) UAV top view

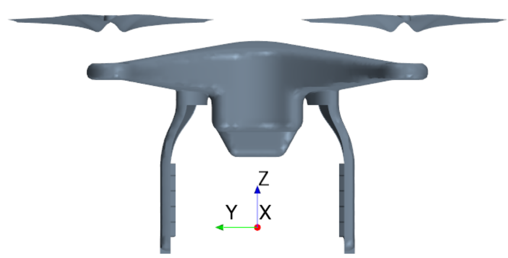

(b) UAV front view

Figure 2.2: UAV model used in the present study shown in (a) top view and (b) front view.

2.2.2 Domain Setup

The STAR-CCM+ documentation recommends a bullet shaped domain for flows within the subsonic regime having Mach numbers equal to or less than 0.3 [30].

Previous studies of rotors have achieved good results utilizing $10D$ for the diameter of the spherical end of the domain, and a downstream length of $20D$ [30, 31]. An image of the overall domain can be seen in Fig. 2.3a, where the small circular object inside the domain is the rotating cylinder containing the rotor.

To prescribe motion to the rotor, the cylindrical volume seen in Fig. 2.1b extending 0.003 m past the blade tips, 0.005 m forward from the base of the rotor, and 0.015 m backward from the base of the rotor, was created. The distance extending beyond the blade tips was recommended in existing literature [30], with the other dimensions modified to fit the rotors used here. This image also denotes the clockwise rotation assigned to this rotor. This creates two separate regions for the domain: the fluid region which subtracts the rotating volume, and the rotating region which subtracts the rotor geometry. A sliding mesh interface was created between the outer boundary of the rotating region and the subtracted surface of the fluid region to allow information to pass from one domain to the next via linear interpolation, creating a unified flow field. Sliding meshes have been used in many CFD simulations for prescribing rotational motion [2, 19, 30, 32, 33, 34].

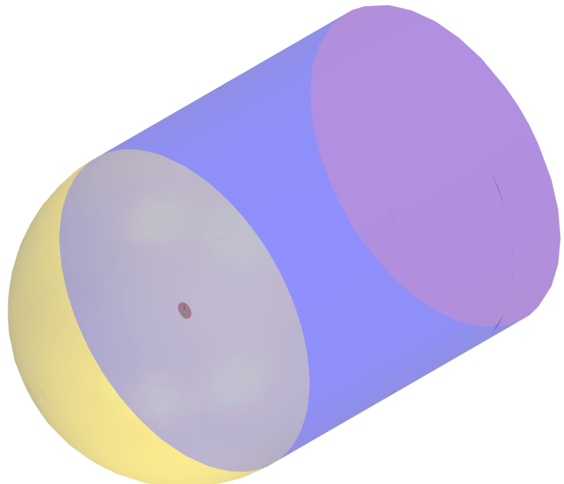

(a) Overall domain

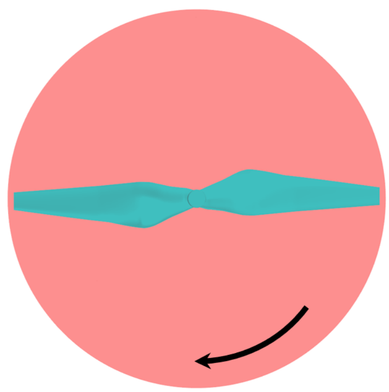

(b) Rotating cylinder

Figure 2.3: (a) Bullet shaped domain used for single rotor simulations and (b) rotating cylinder used to prescribe motion to rotor.

The same type of domain was also used for the dual rotor case. Since the effective diameter was doubled by the addition of a second rotor, the diameter of the spherical end of the domain and downstream length were both doubled to $20D$ and $40D$, respectively. Fig. 2.4a shows the overall domain, with both rotating cylinders containing the rotors visible inside the domain.

Fig. 2.4b shows the two cylindrical volumes used to prescribe motion to the rotors. Once again, these volumes extended 0.003 m past the blade tips [30], 0.005 m forward the base of the rotor, and 0.015 m backward from the base of the rotor. These volumes were separated such that the distance between the blade tips was $0.05D$ apart. This image also denotes the clockwise rotation given to the right rotor, and the counter-clockwise rotation given to the left rotor. This both matches what has been done in experiments [15] and what is standard for the first two rotors in an "x" configuration UAV [2, 4, 6, 16, 35]. This setup creates three separate regions for the domain, one for each rotating cylinder which subtracts the rotor geometries, and one for the fluid region which subtracts the rotating volumes. These regions were also given a sliding mesh interface between the outer surfaces of the rotating regions and the subtracted surfaces in the fluid volume.

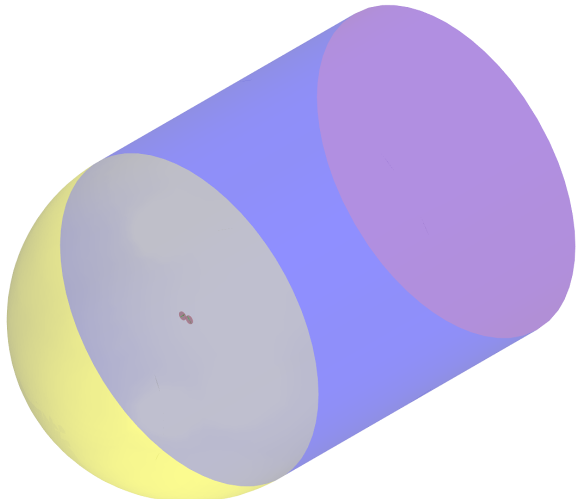

(a) Overall domain

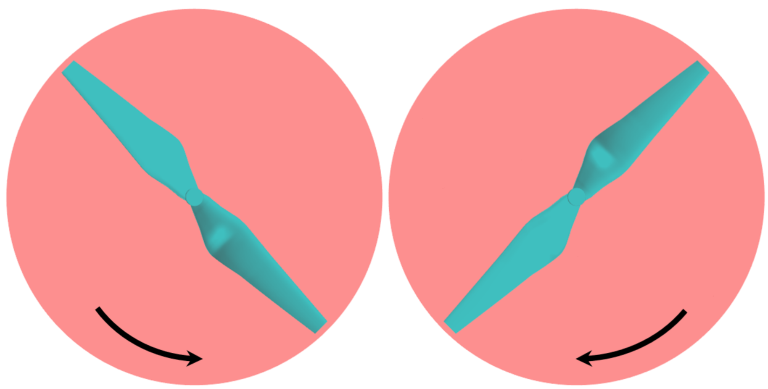

(b) Rotating cylinder

Figure 2.4: (a) Bullet shaped domain used for dual rotor simulations and (b) rotating cylinder used to prescribe motion to rotors.

The overall domain for the full UAV, which will be referred to as the fluid region going forward, was left to the same dimensions as the dual rotor case as the effective diameter did not change with the addition of two more rotors in the present configuration. The spherical end and downstream length remained at $20D$ and $40D$, respectively. The difference in this case is that this region no longer subtracted the rotating cylinders and a new region was added. A cylindrical volume with a diameter of 0.800 m was created, and set to extend 0.100 m forward the base of the rotor and

0.350 m backward. This region, which will be referred to as the overset region going forward, was used to subtract the fuselage of the UAV and the rotating regions in place of the fluid volume. An overset mesh interface was then created between the overset region and the fluid region. An overset mesh, or Chimera grid, is an overlapping mesh technique that allows the interior mesh to move within the stationary background mesh. Information is passed from one mesh to the next via linear interpolation, connecting the meshes to become one continuous flow field. This technique not only allows for more complex motions than standard methods, but also allows for parts of the domain to be moved or replaced without having to remesh the other parts [36]. This method of meshing has been used in many rotorcraft simulations [4, 16, 20, 31, 37]. Fig. 2.5a shows the domain setup for the baseline UAV case, where the UAV is hovering far from any surfaces.

To better understand how being in ground effect can affect the UAV, several other configurations were necessary. Starting at a height of 3.0 m, a simulation was set up with the UAV hovering at increments of 0.5 m until reaching ground level, for a total of seven simulations. Following these, one more simulation was setup utilizing the overset mesh to have the UAV translate vertically from a height of 3.0 m to ground level within the 20 revolutions specified. The upper and lower bounds of the simulation domains can be seen in Fig. 2.4b and Fig. 2.4c.

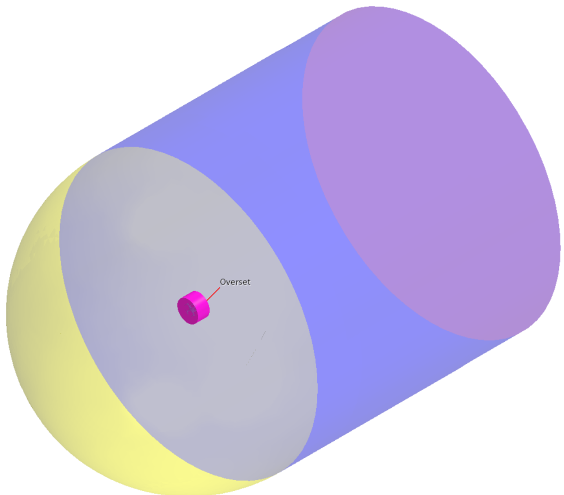

(a) Hovering far from ground

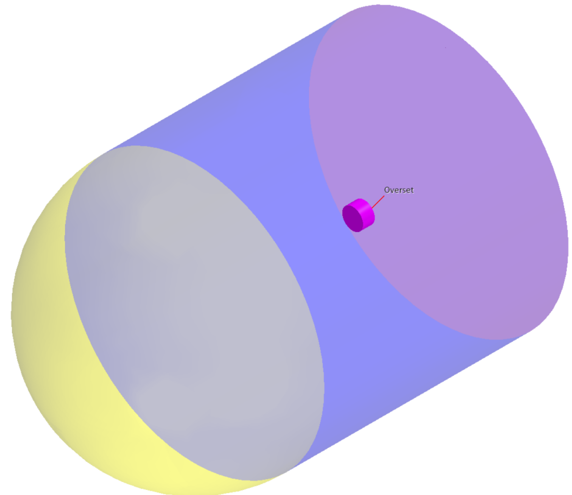

(b) Hovering at 3.0 m

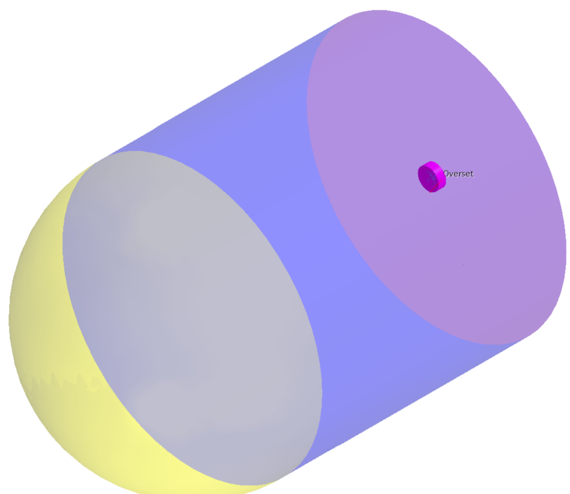

(c) Hovering at ground level

Figure 2.5: Bullet shaped domain used for the UAV when (a) hovering far from ground, (b) hovering at 3.0 m, and (c) hovering at ground level.

Fig. 2.6 shows the four cylindrical volumes used to prescribe motion to the rotors. The dimensions for these volumes are identical to the previous cases. Each volume is centered at the axis of rotation for the UAV arms. This figure also denotes the direction of rotation for each rotor, where two opposite pairs of counter-rotating rotors are used to counteract each rotors angular momentum. This figure also denotes the direction of flight for this configuration. The full setup creates six separate regions within the domain: the four rotating cylinders which subtract the rotors, the overset region which subtracts the four cylinders and the UAV fuselage, and the fluid region which is the background mesh for the overset mesh interface.

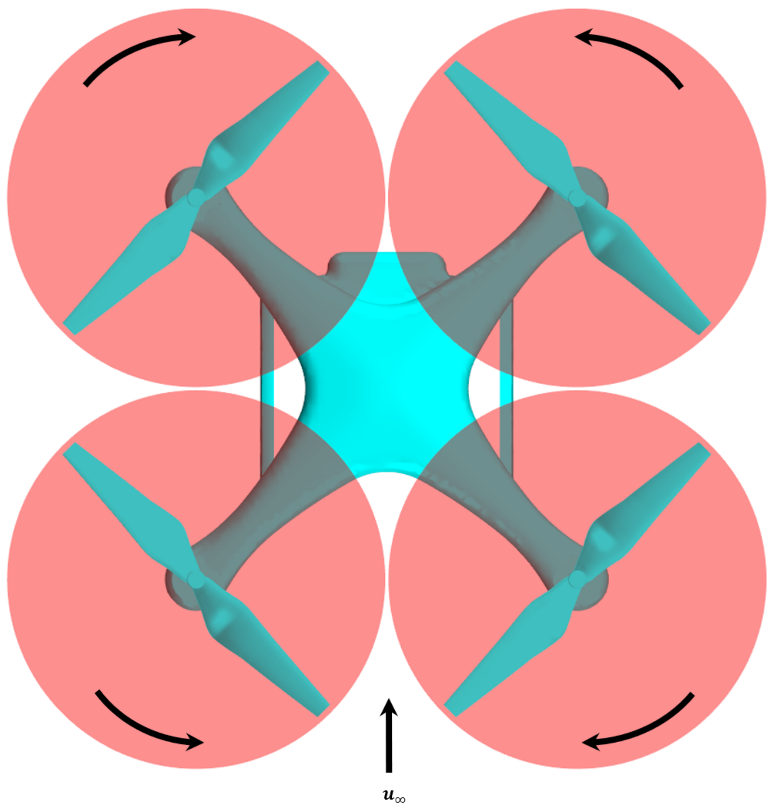

Figure 2.6: Rotating cylinders used to prescribe motion to rotors with rotation directions and direction of flow.

2.3 Boundary and Initial Conditions

The boundary conditions for the domain are also color coded within the images of Fig. 2.3. The yellow surface is defined as a velocity inlet, the blue surface is defined as freestream, the purple surface is defined as a pressure outlet, the red surface is the sliding mesh interface between the two regions, and the cyan surface is defined as a wall.

The initial conditions for the simulation were set to match a rotation rate of 4860 RPM to match that of the experiment referenced for validation [15]. The inlet velocity was set to 0 m/s as the rotor is simulated in hover. The timestep for this simulation was set to 1.0288E-4 s, which corresponds to a recommended 3° of revolution per timestep [30] at 4860 RPM. The total number of timesteps was set to 2400, which represents 20 full rotations. Some existing literature suggests 30 full rotations [38] while others suggest only 10 [30], but from trial and error the simulation seemed to fully converge within 10 revolutions. This ensured that at minimum, 10 fully converged revolutions were available for time-averaging when simulating 20 revolutions. The pressure, static temperature, and turbulence intensity were left to their default values of 0.0 Pa, 300 K, and 0.01, respectively.

The boundary conditions for the dual rotor case were identical to that of the single rotor case. However, it is also color coded in Fig. 2.4, where the yellow surface is defined as a velocity inlet, the blue surface is defined as freestream, the purple surface is defined as a pressure outlet, the red surface is the sliding mesh interface between the two regions, and the cyan surface is defined as a wall.

The initial conditions here were also set to match a rotation rate of 4860 RPM, with an inlet velocity of 0 m/s to represent the rotors in hover. The timestep here was left at the value corresponding to 3° of revolution per timestep [30] at the specified RPM. Since 20 revolutions was deemed sufficient in the previous case, this case also used 2400 timesteps. Finally, the pressure, static temperature, and turbulence intensity were also left to their default values here.

The boundary conditions for the baseline UAV case are nearly identical to previous cases, where they are color coded in Fig. 2.5a. The difference for the UAV cases is that the magenta surface inside the domain represents the boundary of the overset region which is overlapping the background mesh. For all other UAV cases, the boundary conditions have one more difference. The purple surfaces in Fig. 2.5b and 2.5c are set to a wall rather than a pressure outlet. This provides the solid boundary necessary to investigate ground effect.

The initial conditions for all UAV cases were also identical to previous cases, using an inlet velocity of 0 m/s to represent hover, a rotation rate of 4860 RPM for the rotors, a timestep representing 3° of revolution per timestep [30], and a total of 2400 timesteps. The pressure, static temperature, and turbulence intensity were still left to the default values. For the dynamic case, a translating motion specification was given to the overset mesh and was also superposed on the rotation motion specifications for the rotors. This translation was set to have the UAV traverse 3 m in the time it takes for 20 revolutions.

2.4 Mesh Setup

A proper meshing strategy is extremely important for producing accurate results with a RANS simulation. A high mesh resolution is critical in accuracy, but also exponentially increases computational time. Finding the correct balance between a fine enough mesh and fast enough computations is key in engineering. Polyhedral meshes are often better at capturing gradients, however they are computationally expensive compared to trimmed cell meshes. According to the STAR-CCM+ installation guide, the memory requirements for a coupled implicit simulation using a polyhedral mesh is double that of a trimmed cell mesh. Reducing the memory requirements by half is significant, and for this reason, only the rotating region directly around the rotor is discretized on a polyhedral mesh with the rest of the domain being discretized on a trimmed cell mesh.

Referenced literature found that a base size 0.595 m was sufficient for rotors of this size [30]. In the interest of saving computational time, the base size for the overall domain was doubled to a value of 1.19 m. The base size for the rotor was left at the initial value since the doubled value had difficulty meshing the thin trailing edge of the rotors.

The domain, rotating cylinder, refinement cylinder to be discussed later, and the rotor were all imported with a tessellation density set to the STAR-CCM+ very fine setting. To improve the quality of the rotor's surface mesh, a surface wrapping operation was performed. The base size for the surface wrapper was set to 0.595 m [30], with a target and minimum surface size set to 0.04% and 0.02% of the base, respectively.

To provide more detail on the mesh for the rotating cylinder, a surface remesher and prism layer mesher were used in addition to the polyhedral mesher. The target surface size here was set to 10% of the base size, with the minimum surface size set to 1.0% of the base size [30]. The number of prism layers was set to 12, with the prism layer near wall thickness set to 1.0E-5 m and a total thickness of 5.0E-4 m. Three custom controls were set for this mesh, with the first meant to disable the prism layer on the interface of the rotating cylinder. The second control matched the values of the surface wrapping operation, and was meant to better resolve the boundary layer. As before, this changed the target and minimum surface sizes to 0.04% and 0.02% of the base, respectively. Finally, a custom volumetric control was set to improve the mesh away from the rotor surface. For setup simplicity, the volume used for refinement here was used as a standard refinement region for each mesh operation, and was a cylindrical volume set to be $1.25D$ in diameter and extend $1D$ downstream. The custom size for the surface remesher and polyhedral mesher of this region was set to 0.3% of the base [30]. The resulting mesh can be seen in Fig. 2.7a, with a side view showing the refinement region shown in Fig. 2.7b. Fig. 2.7c shows a closeup of the blade surface mesh with prism layers visible.

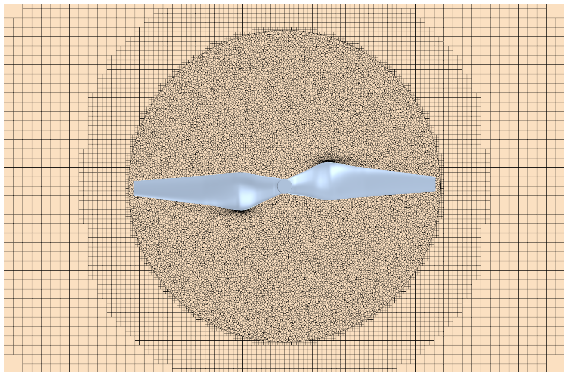

(a) Top view mesh

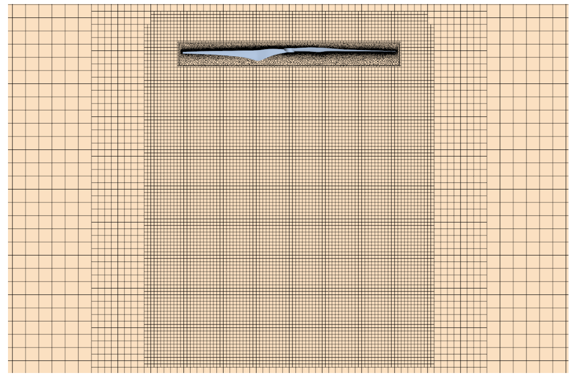

(b) Side view mesh

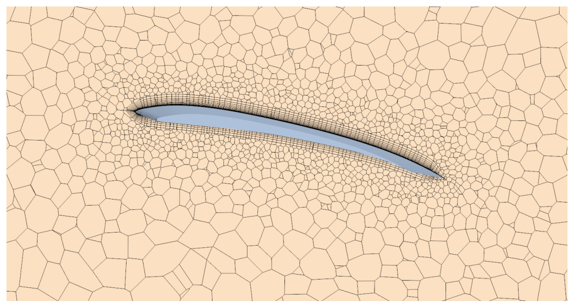

(c) Close-up of blade surface

Figure 2.7: Polyhedral mesh for the rotor seen from (a) top view, (b) side view, and (c) close-up of blade surface.

Typically, a wall $y+$ value of ≤ 5 is a necessity for the SST turbulence model, with a value below one being desirable to resolve the entire viscous sublayer. Some existing literature achieved accurate results with an average value of 3.5 for the wall $y+$ [16]. Others have also relied on the all $y+$ wall treatment to allow for a $y+$ averaging around 30-50 depending on prism layer settings determined using Schlichting's Boundary-Layer Theory [30]. However, this theory is based upon boundary-layer growth over a flat plate. Therefore a wall $y+$ averaging below 1 was used. Looking at Fig. 2.8a, a wall $y+$ of ≤ 1 was gained over the majority of the surface of the rotor. The thin trailing edges and blade tips have slightly higher wall $y+$, but still remain well below 3.5, which can be seen in Fig. 2.8b.

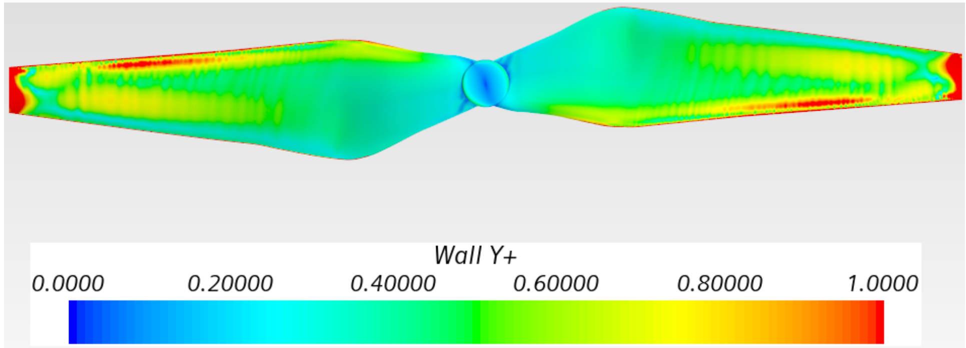

(a) Wall $y+ \leq 1$

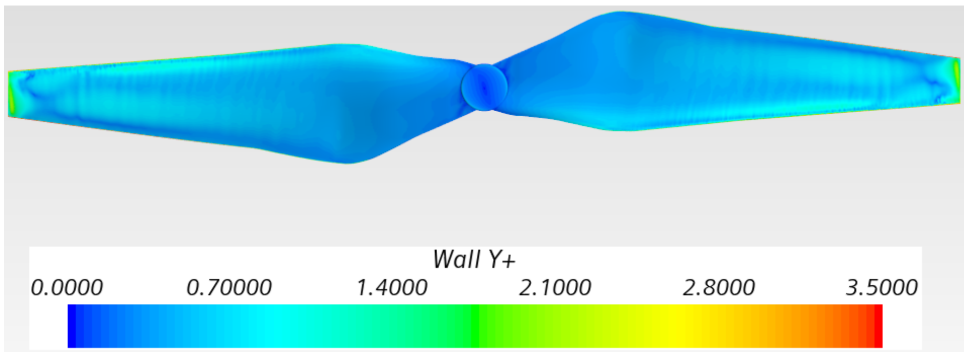

(b) Wall $y+ \leq 3.5$

Figure 2.8: Wall $y+$ for the rotor surface when mapped to (a) ≤ 1 and (b) ≤ 3.5.

Going into more detail for the overall domain mesh, a surface remesher was used in addition to the trimmed cell mesher. The target surface size was set to 10% of the base size, with the minimum surface size set to 1% of the base size. Three custom controls were set. The first was for the cell size at the surface of the domain, where target surface size was set to equal roughly twice the diameter of the rotor. This large of a cell is acceptable to resolve the freestream region. The next custom control used the refinement region to set a target surface size of 0.3% of the base to better resolve the wake region [30]. The final custom control was for the sliding mesh interfacing surface, which was set to 0.15% of the base size. This value was set in such a way to match the cell size to that of the rotating cylinder that had half the base size, as this is necessary for the interpolation between meshes. Fig. 2.9 shows the completed mesh for the overall domain, which shows the highest density of cells near the rotors, and resolution being reduced incrementally when approaching the boundaries. The mesh in this image was rotated 90° in the interest of saving space. However, the z-axis shown in the bottom left corner of the figure is referenced as the vertical axis for all simulations.

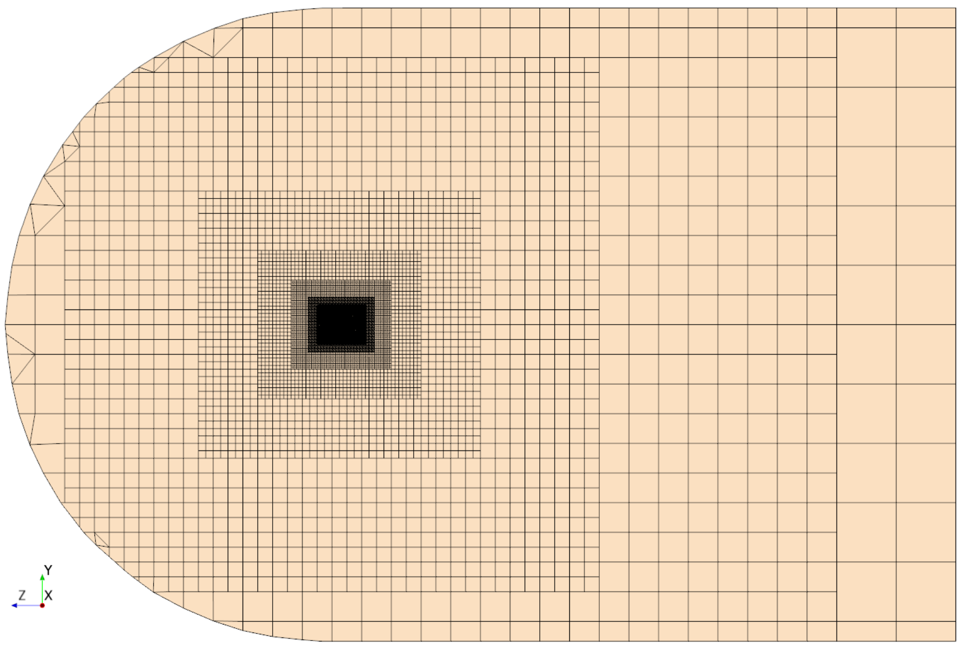

Figure 2.9: Cross-sectional image of the trimmed cell mesh used for the overall domain.

A mesh dependency study was conducted on the single rotor case to ensure the mesh was significantly resolved to accurately predict the thrust. The initial mesh will be labeled M1 going forward. For the mesh refinement, dubbed M2, the base size for the outer domain and the rotating cylinder was halved. This increased the number of cells from 5,872,640 cells to 22,866,177 cells. Zhou et al. state that the rotors used in the present work "can provide a 3.0 Newton thrust at rotation speed of 4860 RPM [15]." Similarly, another study by BYU using identical rotor models found a thrust of 3.123 N using a RANS method [30]. Since the thrust was given in these studies in absolute values rather than coefficients, the thrust going forward will be reported in the same way. Table 2.1 shows the thrust time-averaged over the last 600 timesteps when compared to the expected thrust and the BYU thrust. This thrust is also comparable to the thrust produced by DJI rotors that these models are based on [39]. M1 predicted a thrust of 3.169 N, resulting in a 5.625% overshoot compared to the expected value and a 1.473% overshoot compared to the BYU simulation. M2 predicted a thrust of 3.154 N, resulting in a 5.150% overshoot and a 0.9926% overshoot compared to the two referenced cases. While M2 showed a better thrust prediction, it also shows diminishing returns. With less than half a percent reduction in error on both counts at the cost of nearly four times the number of cells, M1 was deemed mesh independent.

Table 2.1: Mesh dependency study results.

Mesh	Time-Averaged Thrust (N)	Expected Thrust (N)	BYU Thrust (N)	Expected Percent Error (%)	BYU Percent Error (%)
M1	3.169	3.0	3.123	5.625	1.473
M2	3.154	3.0	3.123	5.150	0.9926

Following this, a timestep dependency study was conducted on M1, which is referenced as T1 for this study. The timestep was reduced to represent 2° of revolution per timestep, and was dubbed T2. This corresponds to a timestep of 6.8587E-5 s. This also required an increase in number of timesteps to 3600 to reach the 20 full revolutions desired. Table 2.2 shows the computational thrust time-averaged over the last 600 timesteps when compared to expected thrust of 3.0 N given by Zhou et al. and the thrust found by BYU for both temporal resolutions [15, 30]. The overshoot of thrust prediction slightly increased for this simulation from 5.625% to 5.891% compared to the expected value, and from 1.473% to 1.729% compared to the BYU value. However, with the change in error being on the order of a fifth of a percent, T1 was deemed sufficient.

Table 2.2: Timestep dependency study results.

Mesh	Time-Averaged Thrust (N)	Expected Thrust (N)	BYU Thrust (N)	Expected Percent Error (%)	BYU Percent Error (%)
T1	3.169	3.0	3.123	5.625	1.473
T2	3.177	3.0	3.123	5.891	1.729

As the initial mesh and timestep were deemed sufficient in the dependency studies for the single rotor case, they were used for all following cases without repeating the studies. Therefore, the mesh remained largely the same for the dual rotor case, outside of the domain being doubled in size and every other meshing operation being required to be done twice. The overall domain was discretized on a trimmed cell mesh, with the rotating cylinder being discretized on a polyhedral mesh. The base size for the rotor meshes and domain mesh was still set to the 0.595 m and 1.19 m, respectively [30]. All parts in this simulation were also imported with the same tessellation density set to the STAR-CCM+ very fine setting, with the rotor surface mesh again being improved by the surface wrapping operation discussed previously.

The mesh for the rotating cylinders utilized the surface remesher and prism layer mesher in addition to the polyhedral mesher. All settings were set identical to the previous case, which resulted in the mesh seen below in Fig. 2.10. The top view of the rotor mesh can be seen in Fig. 2.10a, with a side view showing the wake refinement seen in Fig. 2.10b.

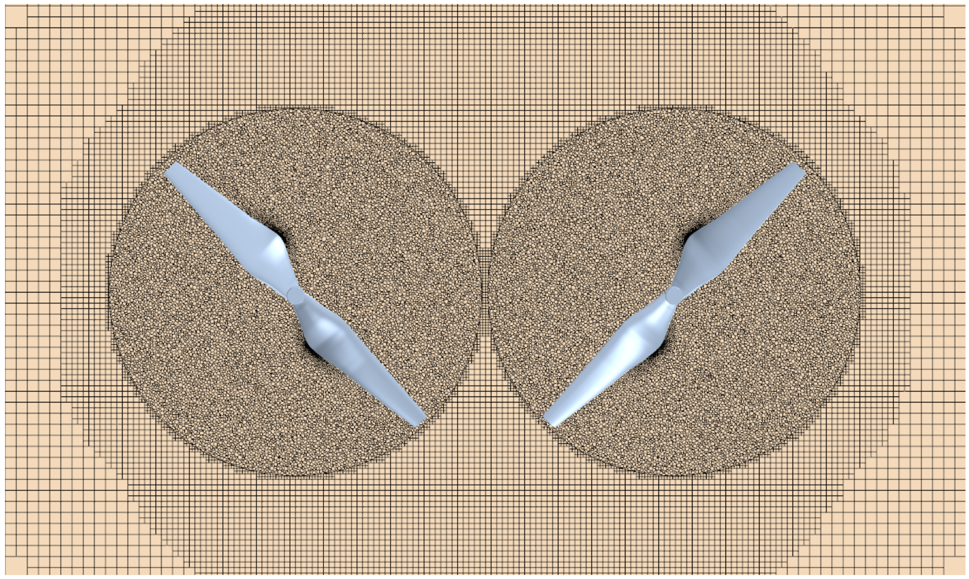

(a) Top view mesh

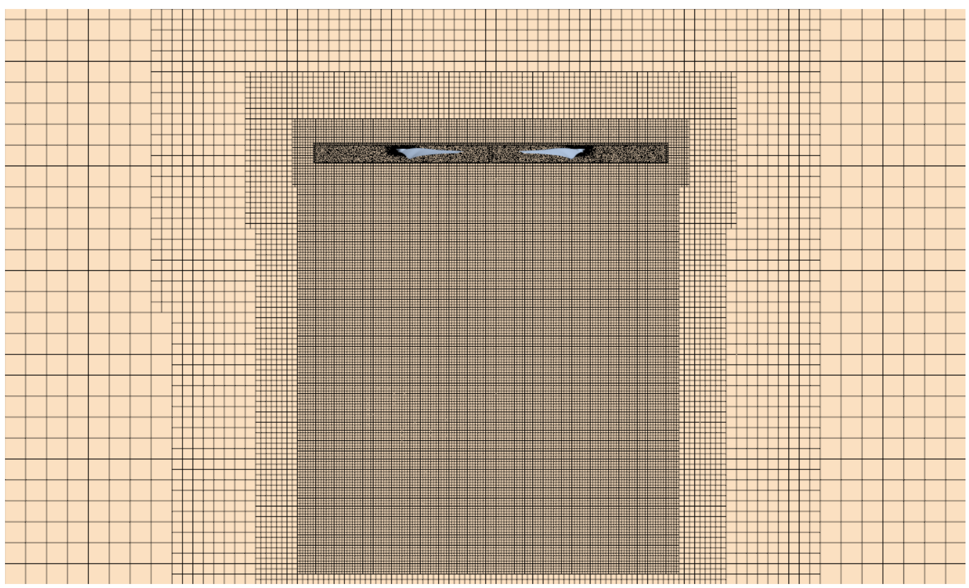

(b) Side view mesh

Figure 2.10: Polyhedral mesh for the rotor seen from (a) top view and (b) side view.

Fig. 2.11a shows the wall $y+$ distribution on the surface of the blade when compared to a value of one. This shows that a value below one was achieved over a majority of the surface of the blade, excluding the blade tips and some locations along the thin trailing edge of the blades. This ensures that the mesh should still be able to resolve a majority of the viscous sublayer. Fig. 2.11b shows that the entire wall $y+$ distribution is well below 3.5, which was referenced from other published work [16].

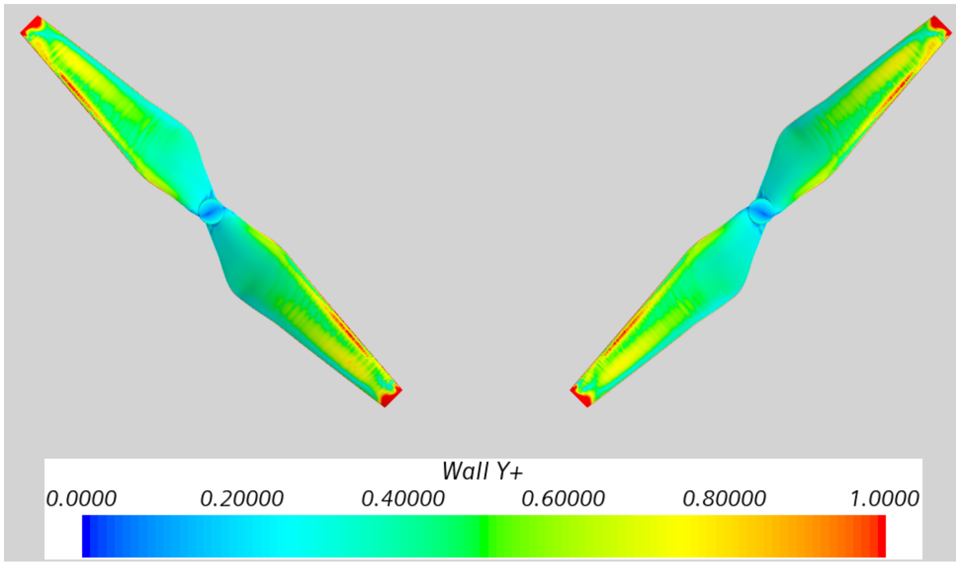

(a) Wall $y+ \leq 1$

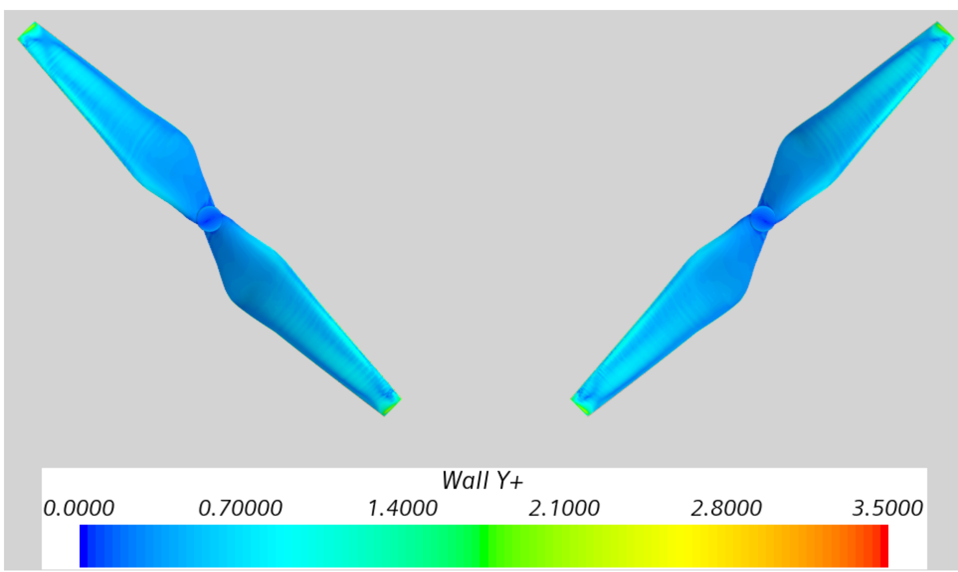

(b) Wall $y+ \leq 3.5$

Figure 2.11: Wall $y+$ for the rotor surfaces when mapped to (a) ≤ 1 and (b) ≤ 3.5.

The mesh for the overall domain also kept most of the same settings as the previous case. The only difference being the refinement cylinder being set to a diameter of $2.5D$

and extending $2D$ downstream. To ensure the difference in base size between this mesh and the rotating cylinder mesh wouldn't cause interpolation issues on these sliding mesh interfaces, the percent of base size used for the custom controls on the subtracted surface in the domain was set to half that used in the custom control for the outer surface of the rotating cylinder. This ensured the cell sizes matched on these interfaces in the same way as the previous case. The resulting mesh can be seen in Fig. 2.12. This mesh setup produced a volume mesh containing 13,657,301 cells, which is slightly more than double the mesh for the single rotor.

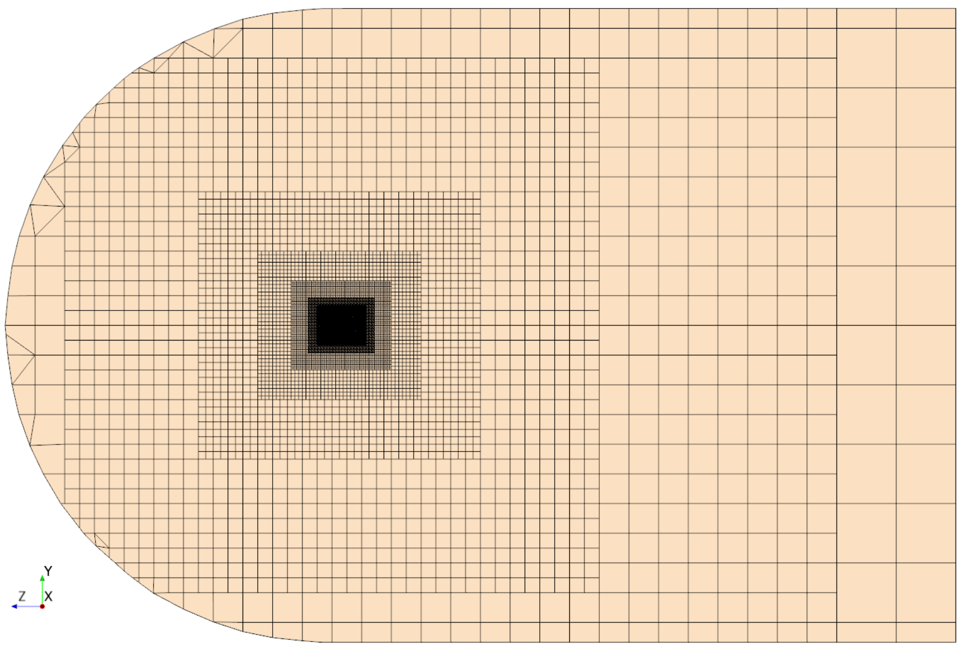

Figure 2.12: Cross-sectional image of the trimmed cell mesh used for the overall domain.

While a majority of the mesh settings used for the full UAV case remained the same as they were in the dual rotor case, the overall structure of the mesh changed in this case. The overset region was meshed with a trimmed cell mesher and surface remesher with the same base size and numerical values previously used for the overall domain. However, since this region now contained the UAV fuselage, a prism layer mesher was added. The prism layer near wall thickness was set to 1.0E-5 m, with a total thickness of 5.0E-4 m, and a total of 12 prism layers. A custom control setting the cell size of the interfacing surface was still set to 0.15% of the base size to match the cell size of the rotating cylinders. Another custom control disabled the prism layer on all surfaces except for the UAV fuselage. The final custom control used the refinement volume to change the cells to 0.3% of the base. The polyhedral mesh for the rotating cylinders were meshed with identical settings as the previous cases. A horizontal slice showing the resulting mesh for the overset region and rotating cylinders overlapping the background mesh can be seen in Fig. 2.13.

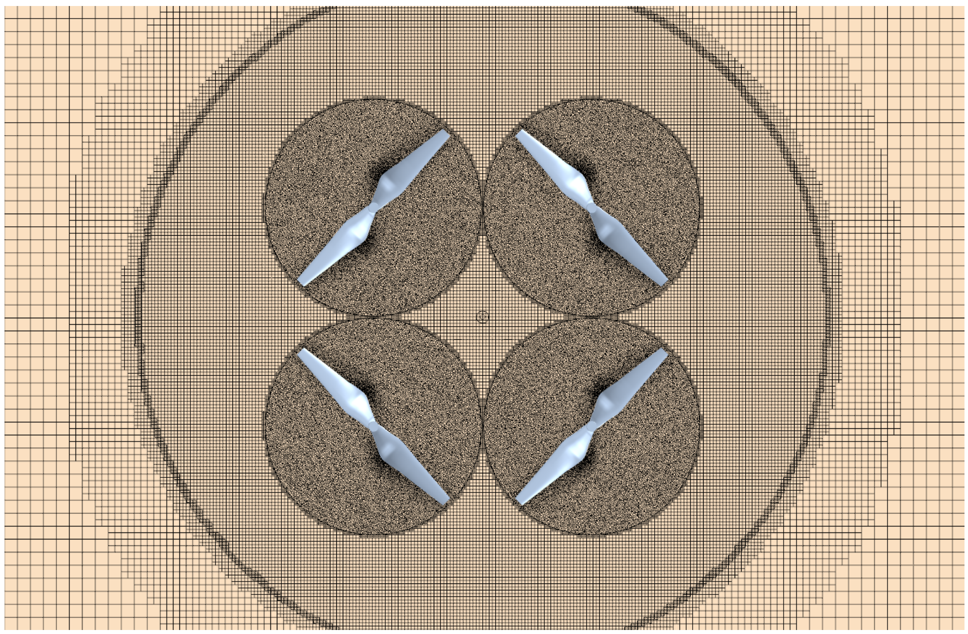

Figure 2.13: Top view of overset mesh for UAV.

For overset meshes, the background mesh that is being moved through must have the same cell size as the overset mesh. For consistency across all UAV simulations, the wake refinement region was extended to a length of 3.0 m to cover the maximum range of motion for any case. Fig. 2.14a shows a zoomed vertical slice at the front rotors of the baseline hovering case overlapping the background mesh. Fig. 2.14b shows the same vertical slice, but for the hovering at 3.0 m case. Finally, Fig. 2.14c shows the same slice again for the hovering at ground level case. The overset region was made shorter for this final case to allow the UAV to be placed in a landed position without having part of the overset region exist outside of the background mesh.

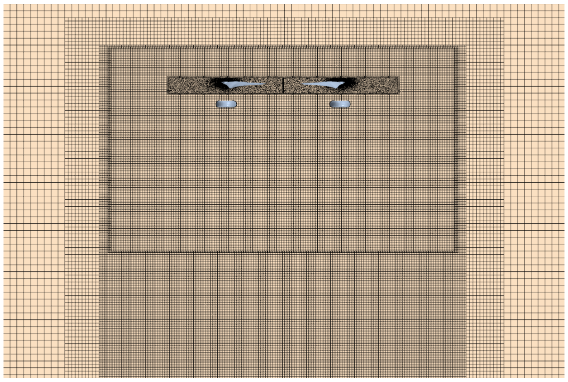

(a) Side view of hovering far from ground mesh

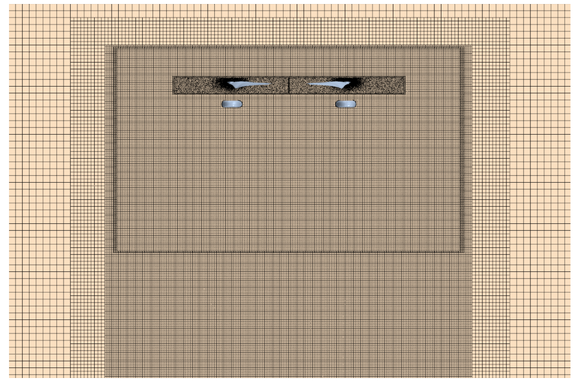

(b) Side view of hovering at 3.0 m mesh

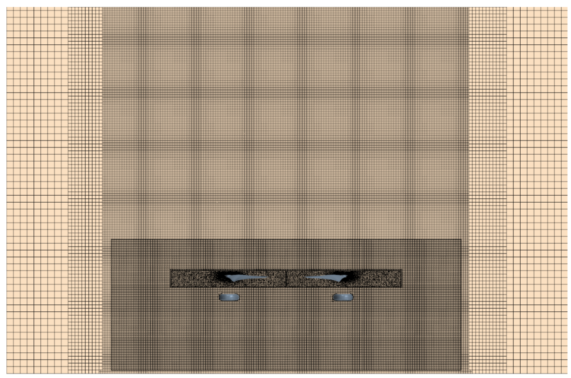

(c) Side view of hovering at ground level mesh

Figure 2.14: Closeup view of overset mesh for (a) hovering far from ground case, (b) hovering at 3.0 m case, and (c) hovering at ground level case.

Fig. 2.15 shows the wall $y+$ values for the UAV rotors and fuselage. The prism layer settings resulted in a wall $y+$ of less than one over the majority of the surface of the fuselage and blades, with a value of less than 3.5 [16] for the entirety of the surfaces. This ensures that the viscous sublayer should be resolved for the rotors as well as the fuselage of the UAV.

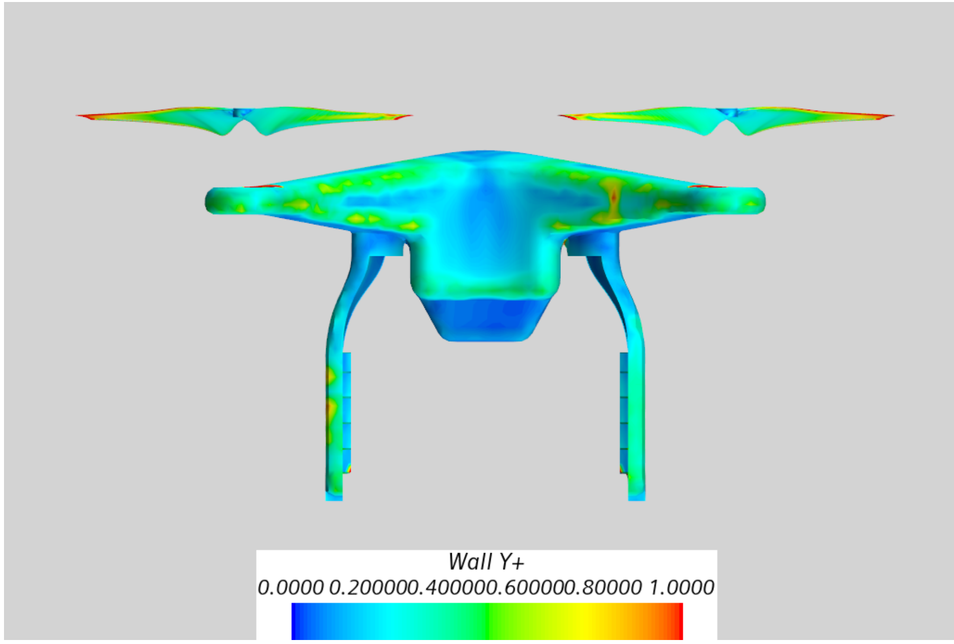

(a) Wall $y+ \leq 1$

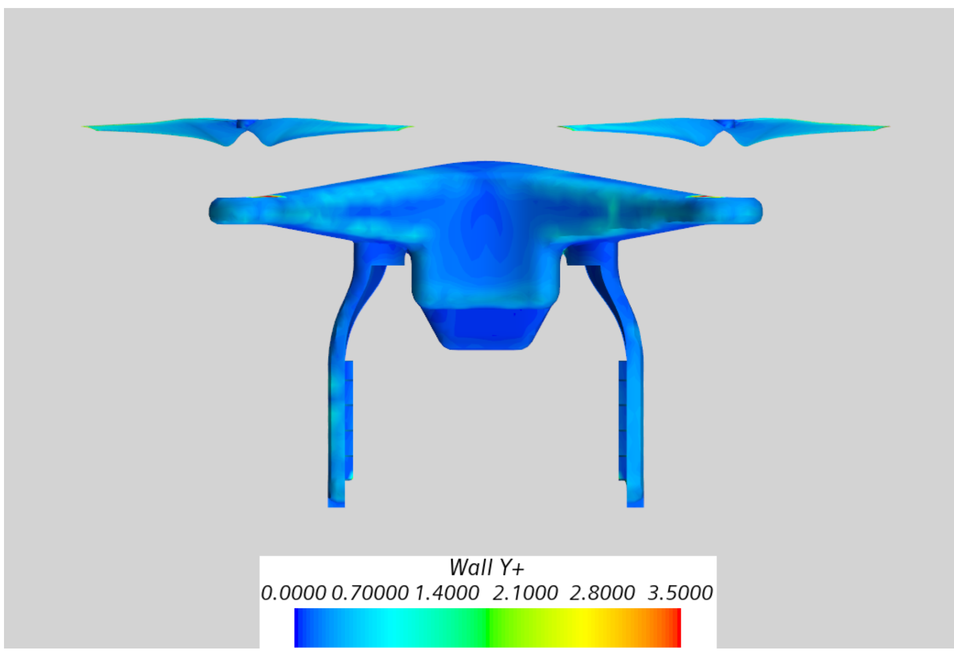

(b) Wall $y+ \leq 3.5$

Figure 2.15: Wall $y+$ for the UAV rotor/fuselage surfaces when mapped to (a) ≤ 1 and (b) ≤ 3.5.

The background fluid domain was left with identical mesh settings to the overall domain in the previous cases, only with the larger refinement volume for the custom control. In each of these cases, the background fluid domain and the refinement region are moved, while the UAV mesh remains stationary. This is because the convenience of overset meshing allows for the more time consuming parts to mesh to remain unchanged while the background mesh can be moved and remeshed several times. Fig. 2.16a shows a vertical slice of the background mesh for the baseline case where the UAV is hovering far from any solid boundaries. The increased refinement region can be seen in this figure. Fig. 2.16a shows a vertical slice of the background mesh for all following cases. The first configuration after the baseline case moved only the background mesh to position the UAV 3.0 m above the ground, leaving the refinement volume in place. Each successive scenario moved both the background mesh and refinement region 0.5 m until the UAV was in a landed position. The top boundary case was also used for the landing case, as the refinement region was already in place to have the overset mesh translate vertically through cells of the correct size. The mesh settings resulted in a mesh with approximately 83 million cells for each scenario.

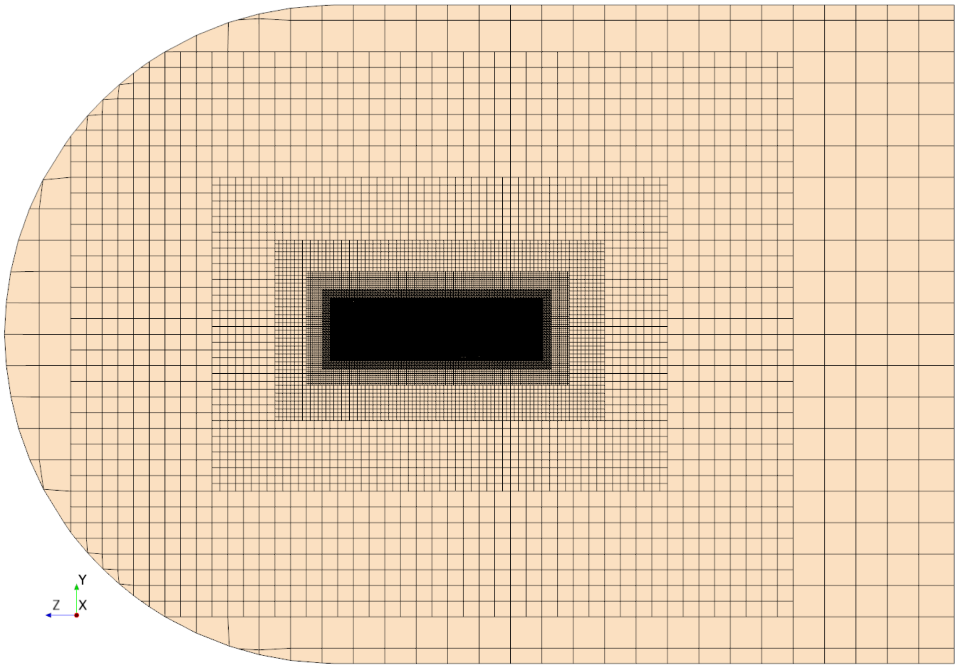

(a) Domain mesh for hovering far from ground case

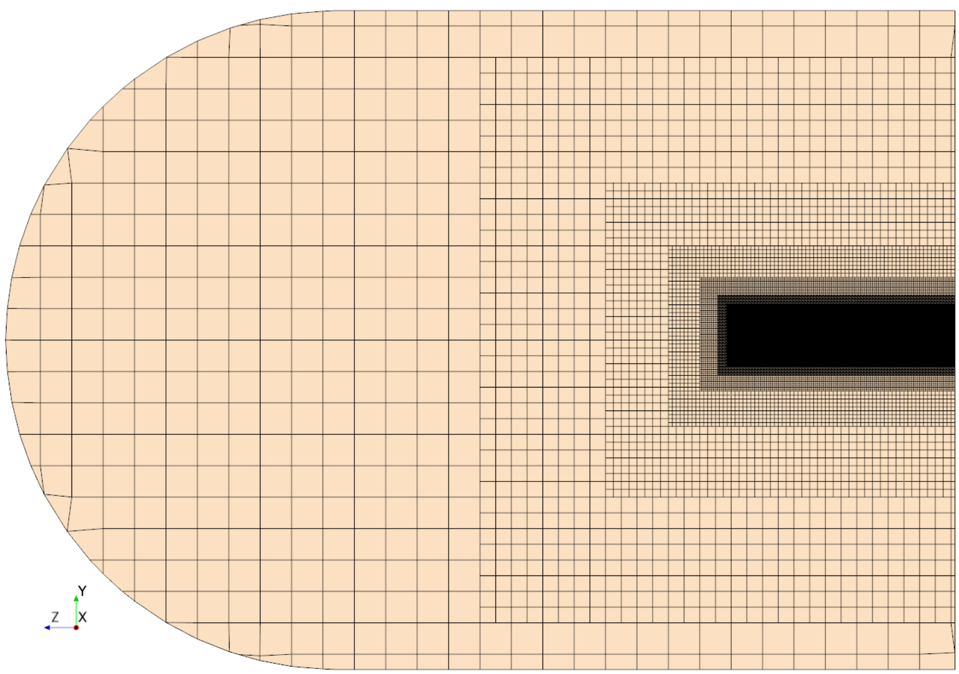

(b) Domain mesh for all hovering near ground cases

Figure 2.16: Cross-sectional image of the trimmed cell mesh used for the overall domain for (a) hovering far from ground case and (b) all hovering near ground cases.

CHAPTER 3: MODEL VALIDATION

3.1 Single Rotor Case

Possibly the most important factor in judging the accuracy of a CFD model is model validation. Building a simulation from the ground up requires validation at each step, and comparisons to experiments are key. The first step in this case was to accurately model a single rotor.

The following results are for mesh M1 with timestep T1 for the single rotor case, as they were deemed to be sufficient for the purposes of this study. As previously stated, a stopping criteria of 2400 maximum steps was used to represent 20 full rotations at $3°$ per timestep. The maximum inner iterations were left at the default of 5 in the interest of lowering computational time. The main parameter of interest for this simulation was the rotor thrust, and conveniently, STAR-CCM+ has a built-in monitor for the thrust only requiring an input part. The rotor surface was used for the input part, and the plot in Fig. 3.1 was generated. As this is a transient simulation, some fluctuations in thrust are expected as the blade rotates. However, it is clear this value converged as this fluctuation is very minimal for this case.

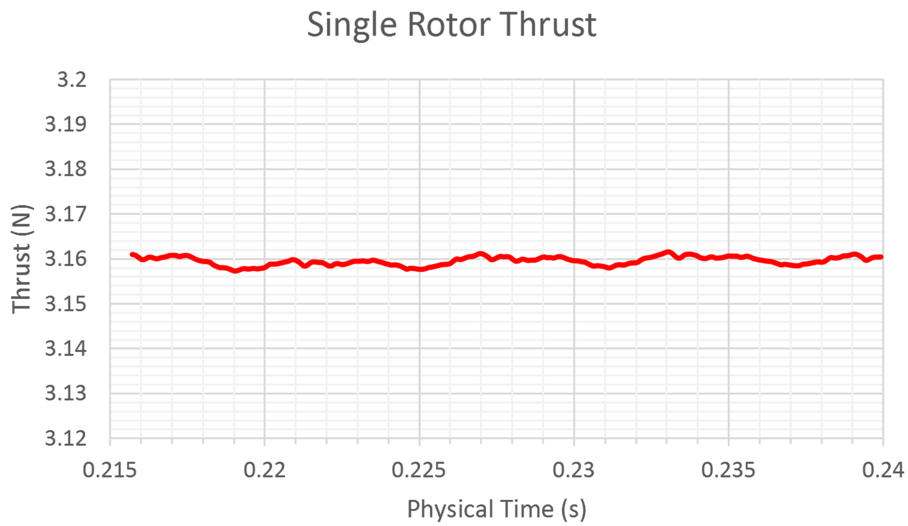

Figure 3.1: Thrust over ∼0.025 s showing approximately 2 revolutions of the Single Rotor.

To determine simulation accuracy, the results were compared to an expected value given in an experimental study by the Advanced Flow Diagnostic and Experimental Aerodynamic Laboratory at Iowa State University. The researchers there used the same model referenced in this paper to manufacture hard plastic rotors using additive manufacturing. They used a high-sensitivity force-moment sensor for the thrust measurements and a high resolution Particle Image Velocimetry (PIV) system seeded by 1 μm oil droplets to generate the more detailed flow field measurements [15]. This method was similar to methods used in other published works [40, 41, 42, 43]. The thrust was also compared to data found in a published RANS study by BYU that used the same rotors as the present work [30]. The thrust gathered from the simulation was time-averaged over the last 600 timesteps where the solution was fully converged without question. An overshoot of approximately 5.625% was found when comparing the computational thrust to expected thrust given by Zhou et al., and an overshoot of approximately 1.473% was found compared to the BYU simulation [15, 30]. This level of error is well within reason for a RANS simulation.

Table 3.1: Comparison for computational thrust.

Mesh	Time-Averaged Thrust (N)	Expected Thrust (N)	BYU Thrust (N)	Expected Percent Error (%)	BYU Percent Error (%)
M1	3.169	3.0	3.123	5.625	1.473

Fig. 3.2 shows the time-averaged k-component of the velocity on a resampled volume that is sliced at the center-plane of the rotor. The k-velocity, as well as all following time-averaged parameters, was averaged every half rotation from 10 revolutions to 20 revolutions. This figure takes the negative z-direction to be positive. A high velocity region is created from the root of the blade to the tip as the flow is convected downward. The wake has a radial contraction at $z/D = 0.25$, denoted by the white arrow, before beginning to expand again. This agrees well with the experimental findings [15] and other computational works [16, 29, 35].

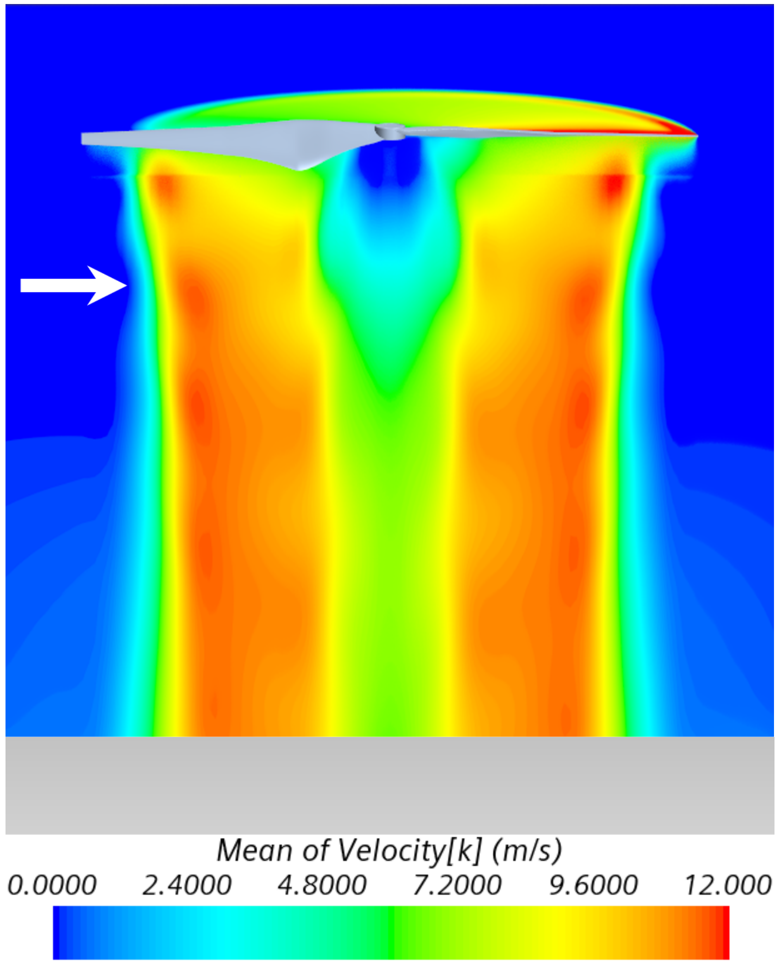

Figure 3.2: Time-averaged k-component velocity contours on a resampled volume.

Fig. 3.3 shows the time-averaged k-component velocity contours on a top view. These figures take the negative z-direction to be positive At $z/D = 0.1$, the velocity contour rear of the rotor is a symmetric circle. This result is expected and matches experimental results. Moving further downstream to $z/D = 1.0$, the symmetric shape begins to break down. Experimental results show the contours take on more of a 'horseshoe' shape at this distance downstream [15], but this simulation shows this beginning to happen closer to $z/D = 1.5$. However, other RANS studies have shown a similar delay [30].

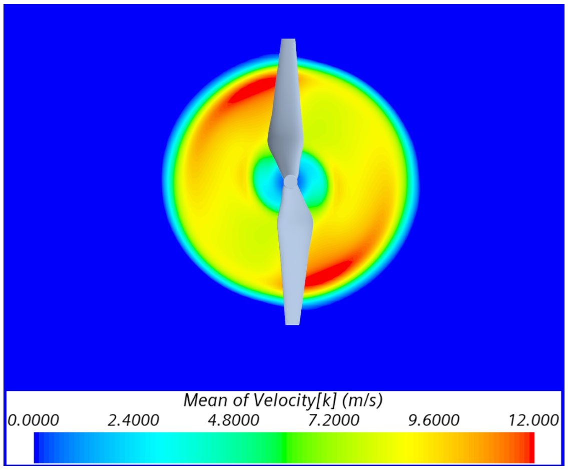

(a) $z/D = 0.1$

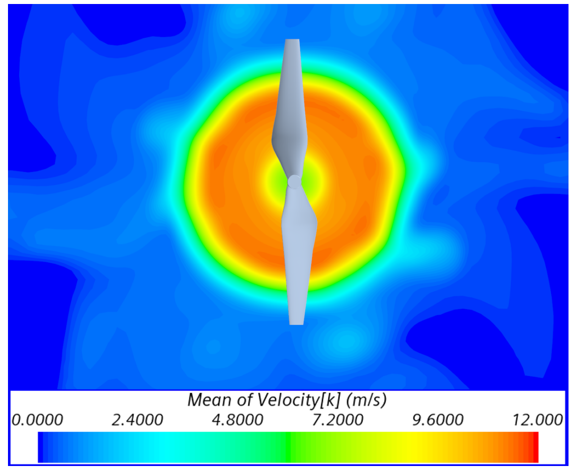

(b) $z/D = 1.0$

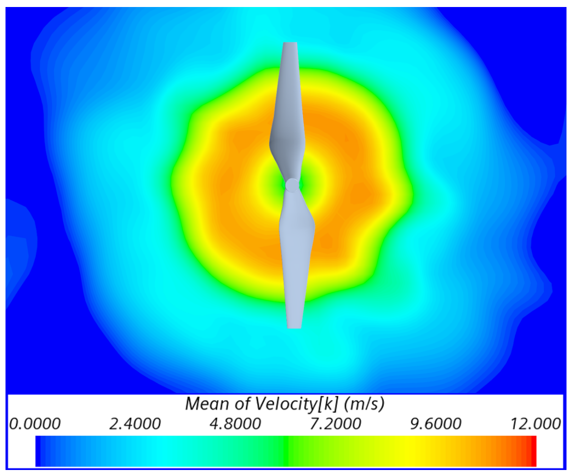

(c) $z/D = 1.5$

Figure 3.3: Time-averaged top view k-component velocity contours at (a) $z/D = 0.1$, (b) $z/D = 1.0$, and (c) $z/D = 1.5$.

Fig. 3.4 shows the instantaneous vorticity magnitude, which highlights the tip vortices as they convect downwards as well as the high vorticity core below the rotor hub. This also shows the formation of shear layers that occur due to the combination of boundary layers from the upper and lower blade surfaces. The first of these shear layers is seen at approximately $z/D = 0.25$, denoted by the white arrow, and the second is seen at approximately $z/D = 0.7$, denoted by the red arrow. This agrees reasonably well with the experimental data, which shows the shear layers at approximately $z/D = 0.25$ and $z/D = 0.5$ [15].

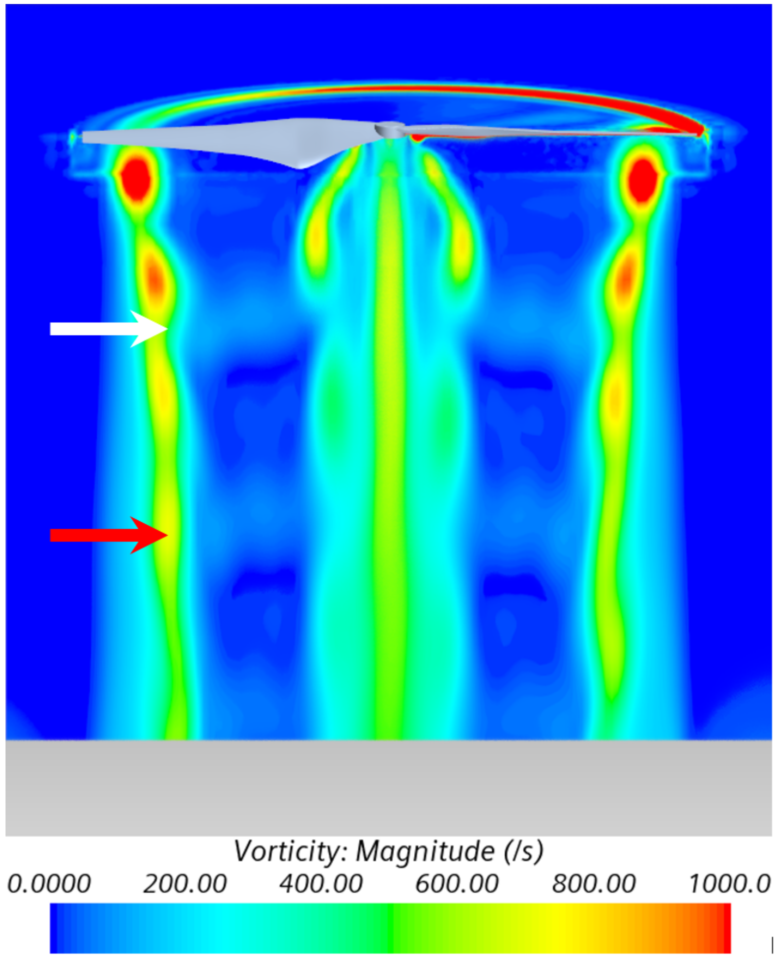

Figure 3.4: Instantaneous vorticity magnitude contours on a resampled volume.

Fig. 3.5 shows the instantaneous i-component vorticity contours taken at the final timestep. The vorticity field matches the trend that is seen in both experiments [15], and other simulations [44], but the vortex cores seem less defined than the aforementioned as they move downwards. However, they initially seem less diffused than seen in other simulations [44]. The lowered definition of the vortex cores further downstream is likely a result of the resolution being lower in the wake region than in the region directly surrounding the rotor tips. This could also be a limitation of using a RANS method. However, the vortices are expected to vanish beyond $z/D = 1.0$ downstream. The results of the simulation agree reasonably well with this, showing no localized vortex core past $z/D = 1.0$.

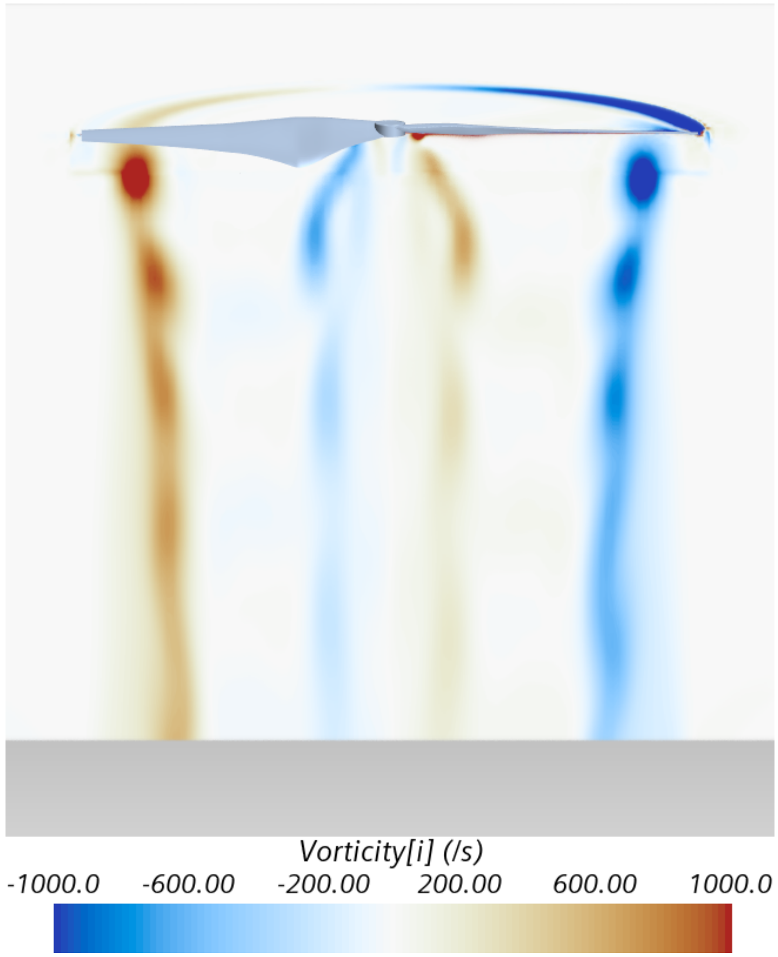

Figure 3.5: Instantaneous i-component vorticity contours on a resampled volume.

Fig. 3.6 shows the Q-criterion isosurface set to a value of 20,000 s^{-1} colored by the k-component velocity contours. This figure takes the positive z-direction to be positive. This visualizations clearly shows the advancing and retreating tip vortices as they progress downwards, which is comparable to what is found in other published works [18, 31, 45]. The positive velocity on the outside of the tip vortices and negative velocity on the inside denotes the direction of vortex rotation, which is counter-clockwise from a frame of reference based on the advancing tip. The reduction in velocity on both sides as the tip vortices progress downwards shows that the rotation is weakening. This image also shows the helical structure of the vortex core beneath the rotor hub. It seems that this helical structure is a result similar to that of tip vortices that are forming at the flared portion of the trailing edge, which is highlighted by the red dashed oval. Finally, Fig. 3.7 shows the instantaneous scalar Q-criterion on the resampled volume. The opacity was lowered for this visualization to better show the helical core and the paths of the tip vortices.

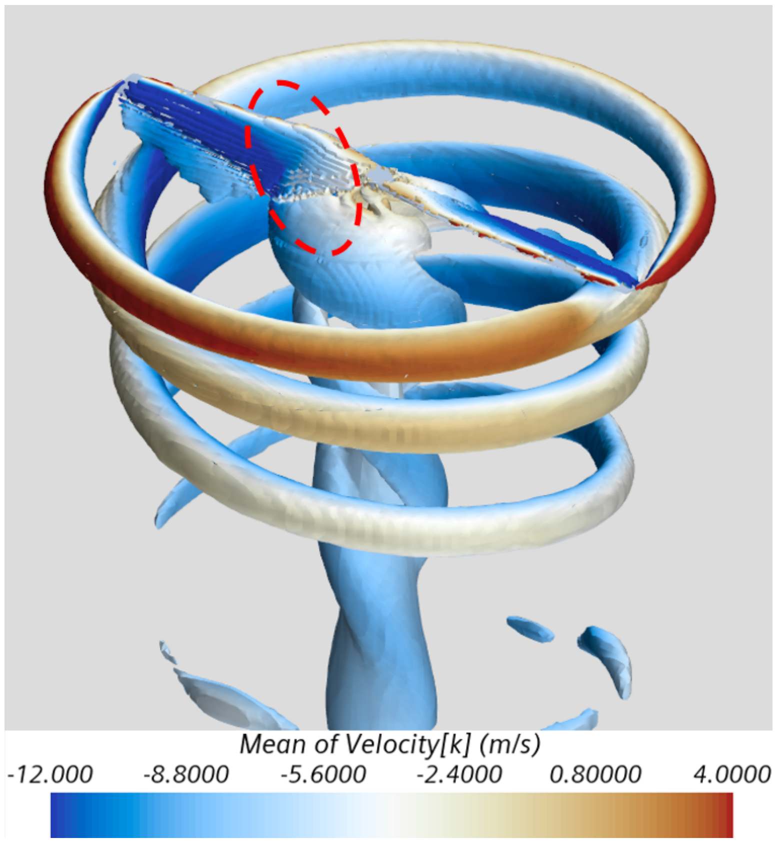

Figure 3.6: Q-criterion isosurface colored by time-averaged k-component velocity contours.

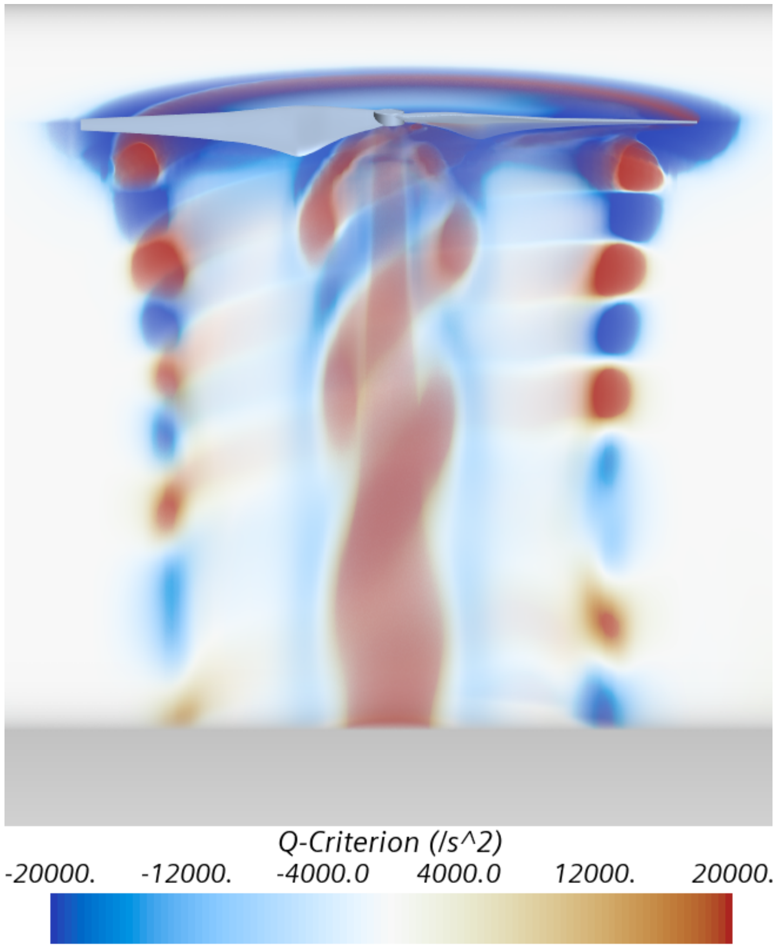

Figure 3.7: Scalar Q-criterion on the resampled volume with lowered opacity.

3.2 Dual Rotor Case

Before moving on to a full UAV case, it was important to ensure the present setup could accurately model rotor-rotor interactions. In this case, two of the same rotors were modeled with a separation distance between rotor tips set to $0.05D$. This tip distance was the minimum distance examined in the experimental case used for comparison [15] as it most accurately represented the tip separation distance seen on the DJI Phantom UAV model used in the later sections.

Once again, the stopping criteria of 2400 timesteps was used to correspond to 20 rotations at 3° per timestep. The maximum number of inner iterations was still left at the default value of 5. Fig. 3.8 shows the plot of the thrust over $\sim$0.025 s which represents approximately 2 revolutions. This plot was generated using the built-in STAR-CCM+ thrust monitor using the right rotor as the input part. A single rotor was used as the input part as the desired parameter to be gained in this simulation is the effect the newly introduced rotor has on the initial rotor thrust. The fluctuations in the thrust are expected with the introduction of the second rotor. A period of the fluctuation is highlighted using the vertical blue lines on the plot, which shows that the period occurs over approximately 0.0062 s. With the timestep representing 3° this period of time corresponds to roughly 180° of rotation. This means the thrust is fluctuating each time the blade tips are passing by one another.

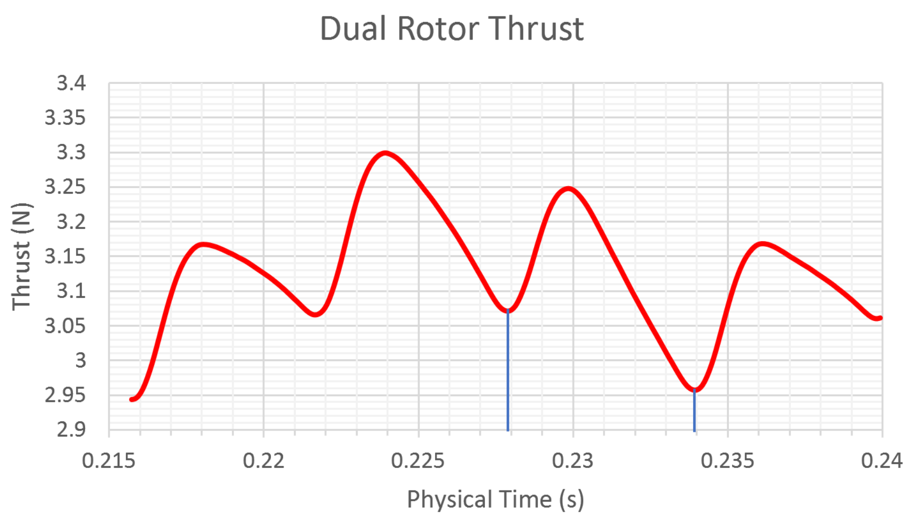

Figure 3.8: Thrust over ∼0.025 s showing approximately 2 revolutions of the Dual Rotors.

The resulting time-averaged thrust from this simulation was compared to the time-averaged thrust from the single rotor simulation in Table 3.2. The rotor in the dual rotor case had a time-averaged thrust of 3.129 N, while the rotor in the single rotor case had a time-averaged thrust 3.169 N. This shows a drop in thrust of 1.256%. This matches well with the experiment referenced in the previous section, where the measured thrust for the case with a separation distance of $z/D = 0.05$ dropped by less than 2% when compared to the time-averaged thrust for the singular rotor [15].

The conclusion that time-averaged thrust is independent of tip separation distance at this rotation speed can be drawn from these results, which agrees with conclusions from other published works [46]. This builds confidence in the simulation's ability to model rotor-rotor interactions.

Table 3.2: Thrust comparison to show effects of additional rotor on time-averaged thrust.

Single Rotor Thrust (N)	Dual Rotor Thrust (N)	Percent Change (%)
3.169	3.129	-1.256

Once again, all time-averaged parameters have been averaged every 180° for the latter 10 revolutions. Fig. 3.9 shows the time-averaged k-component velocity contours on a resampled volume sliced at the center plane of the rotor. This figure takes the negative z-direction to be positive. The introduction of the second rotor seems to cause the wake on the retreating side to be attracted to the adjacent rotor. This has been suggested to be a result of the Coanda effect [15]. The Coanda effect is the tendency of flow to attach to solid surfaces. As this phenomena can occur in gases as well, this conclusion seems reasonable [47]. Interestingly, this trend seems to influence the rest of the wake as well, pulling the central low velocity region as well as the outer high velocity region towards the adjacent rotor. However, the radial contraction, denoted by the white arrow, that occurs at approximately $z/D = 0.25$ is still evident in this case. The location at which the wakes meet in the referenced experimental case is approximately $z/D = 0.3$, where here it occurs closer to $z/D = 0.4$.

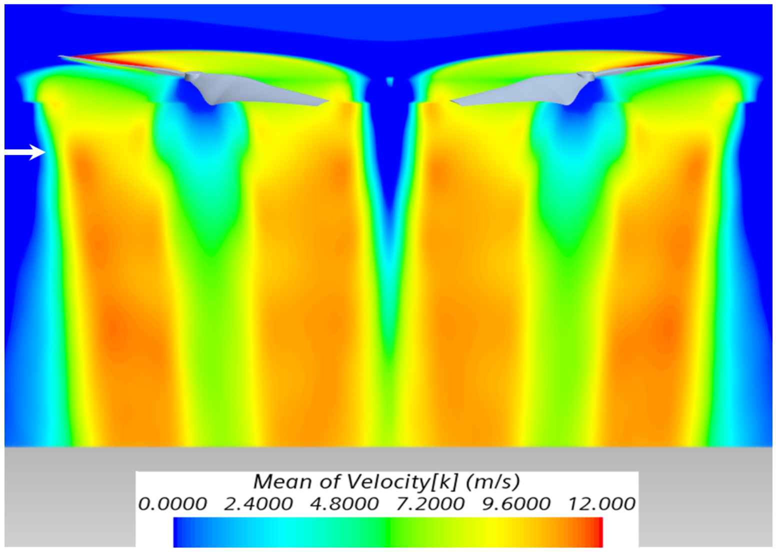

Figure 3.9: Time-averaged k-component velocity contours on a resampled volume.

Moving on to the top view, Fig. 3.10 shows the time-averaged k-component velocity contours on several horizontal slices downstream the rotors. These figures also take the negative z-direction to be positive. In experiments [15] there is an induced upwash that occurs due to the interference of the adjacent rotor that causes a flow separation at a $z/D = 0.1$. However, similarly to previous downstream parameters in this RANS simulation, this phenomena is delayed until a $z/D = 0.4$. Fig. 3.10b shows the induced upwash with a white arrow, and the separated region in the white dashed oval. Other RANS simulations see a similar delay in separation, also occurring at a $z/D = 0.4$ [30], while higher fidelity methods seem to predict more accurate separation [44, 45]. Moving further downstream to $z/D = 1.0$, the simulation shows the flow separation on a more exaggerated scale, but similar to the single rotor case the expected velocity field is delayed to $z/D = 1.5$. Here, the flow breaks down in a similar manner to the single rotor, only with the vortex cores beginning to converge.

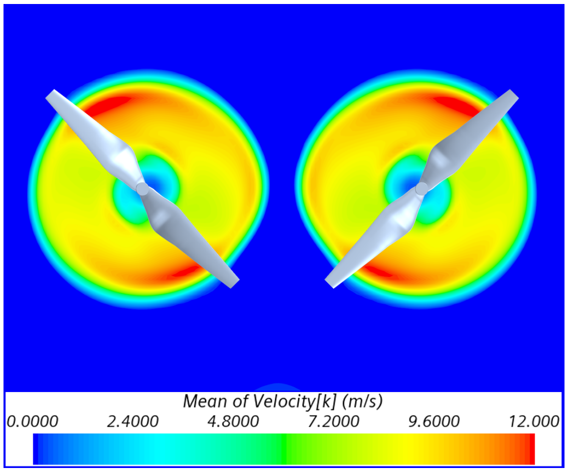

(a) $z/D = 0.1$

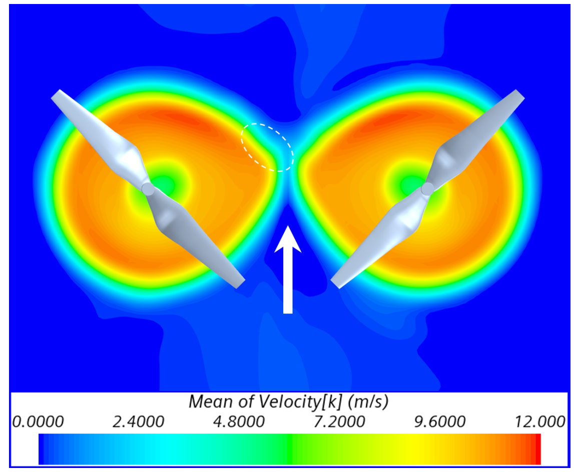

(b) $z/D = 0.4$

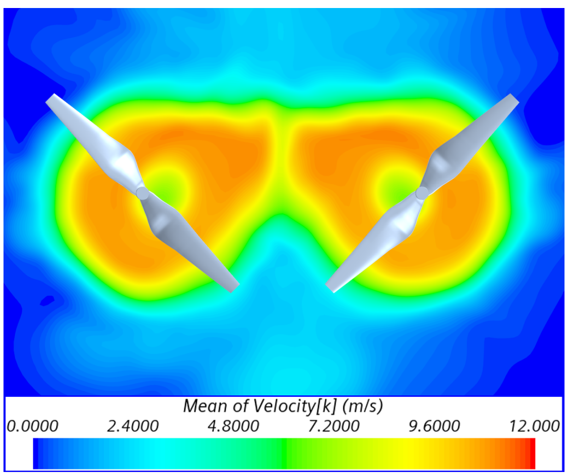

(c) $z/D = 1.0$

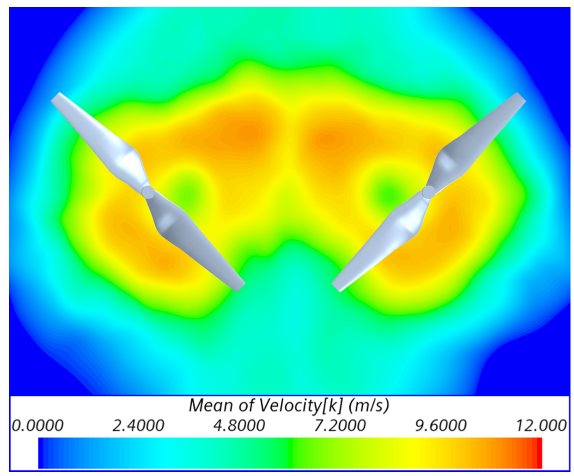

(d) $z/D = 1.5$

Figure 3.10: Time-averaged top view k-component velocity contours at (a) $z/D = 0.1$, (b) $z/D = 0.4$, (c) $z/D = 1.0$, and (d) $z/D = 1.5$.

Fig. 3.11 shows the instantaneous vorticity magnitude contours on the resampled volume. This further shows the trend that the wake is attracted to the adjacent rotor, but also highlights some other interesting phenomena. The retreating tip vortices seem to elongate as they move downwards until they inevitably begin to swirl and combine at approximately $z/D = 0.9$. Even more interesting, the advancing tip vortices shed in a somewhat oscillatory manner. It is possible this is a result of the influence that the second rotor has on the overall trend of the wake flow being attracted towards the adjacent wake. The shear layers here occur at approximately the same downstream length as the single rotor case, and are again denoted by the white arrow for the $z/D = 0.25$ layer and the red arrow for the $z/D = 0.7$ layer. The only difference in this case is that shear layers on the retreating sides are propagating downwards with a slight diagonal trend. This is likely a result of the part of the shear layer nearest to the adjacent rotor feeling the Coanda effect more greatly.

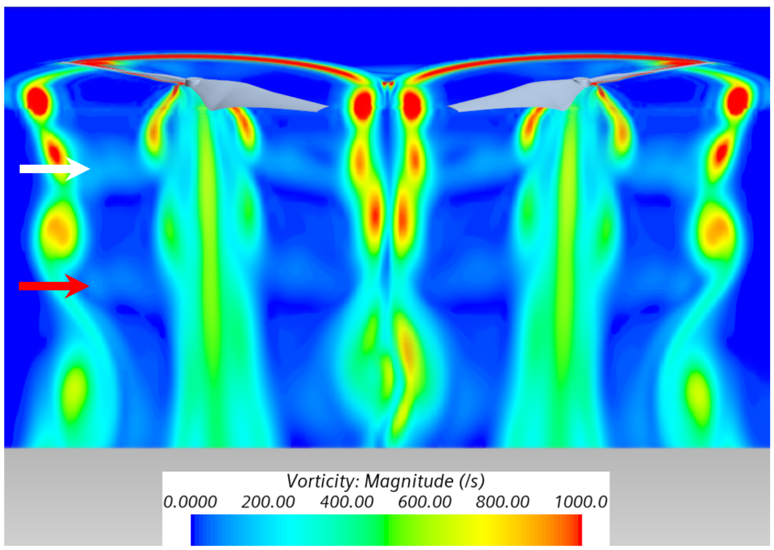

Figure 3.11: Instantaneous vorticity magnitude contours on a resampled volume.

Fig. 3.12 shows the instantaneous i-component vorticity on the resampled volume, and this shows a similar trend to the vorticity magnitude. The retreating tip vortices are elongated and begin to mix, and the advancing tip vortices seem to be affected by the overall trend of the flow being attracted towards the adjacent rotor. The phenomena of the tip vortices elongating is seen in other published works [15, 44]. All tip vortices seem to dissipate slightly faster than seen in the single rotor case.

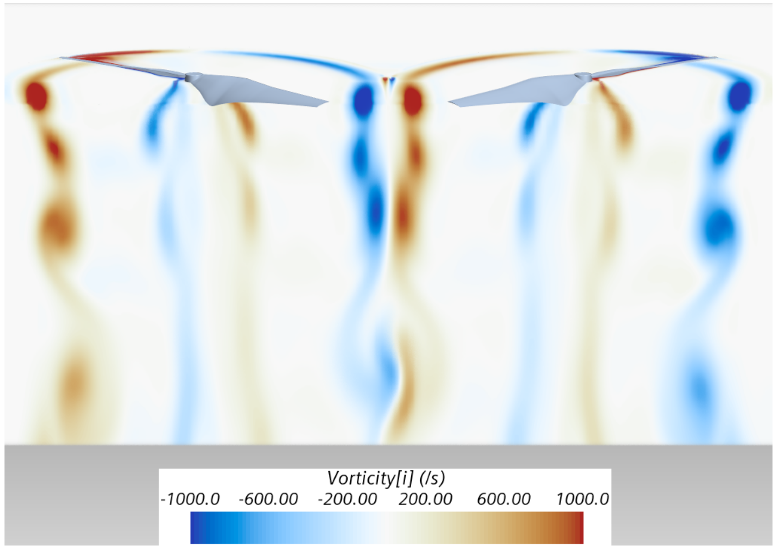

Figure 3.12: Instantaneous i-component vorticity contours on a resampled volume.

Fig. 3.13 shows the Q-criterion isosurface set to a value of 20,000 s^{-1} and colored by the time-averaged k-component velocity contours. This figure takes the positive z-direction to be positive. In the same way as the single rotor case, the z-velocity being positive on the outside of the tip vortices and negative on the inside denotes the direction of their rotation. This visualization also illustrates that the induced upwash and flow separation is delayed until $z/D = 0.4$. Other RANS methods have shown similar trends [30], with higher fidelity methods showing less delayed separation and the formation of more smaller scale vortices [4, 44, 48]. At this distance downstream the retreating tip vortices can be seen interacting in a similar manner to the top view k-velocity contours seen in Fig. 3.10b. The helical center vortex beneath the rotor hub can be seen at a slight angle in this figure, as it is being pulled towards the adjacent rotor. This can be seen better in Fig. 3.14, where the Scalar Q-criterion with lowered opacity is shown. This also better shows the interaction between the retreating tip vortices beginning to occur at $z/D = 0.4$, and also shows that they begin to mix and dissipate as they approach $z/D = 1.0$ as previously suggested.

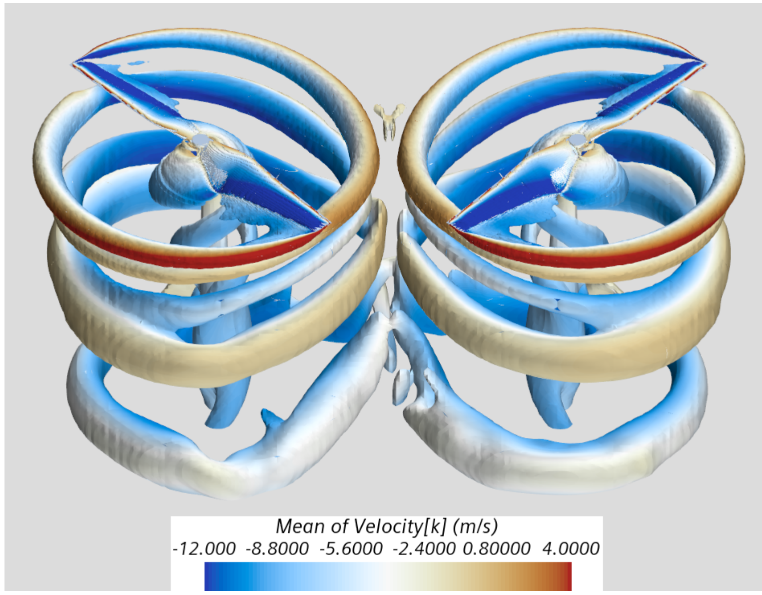

Figure 3.13: Q-criterion isosurface colored by time-averaged k-component velocity contours.

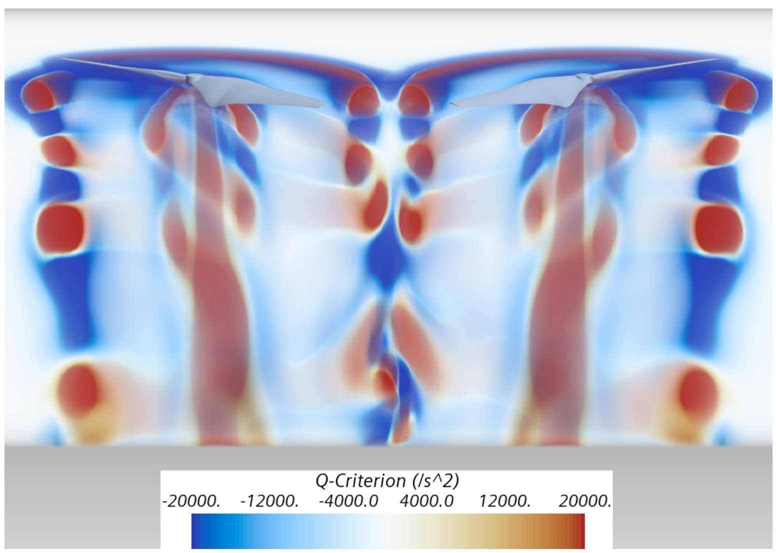

Figure 3.14: Scalar Q-criterion on the resampled volume with lowered opacity.

CHAPTER 4: RESULTS

4.1 UAV Baseline Case

With the CFD framework successfully validated for single and dual rotor cases, this method could be applied to a full UAV to observe how ground effect changes the UAV aerodynamics. However, a baseline case far from any solid boundaries was necessary for comparative purposes. This case, while not directly validated through experiments using identical rotors, can be compared to general trends seen in other computational and experimental works on quadrotor UAV. Here, the stopping criteria was also set for 2400 timesteps, with the default 5 inner iterations per timestep. The thrust over approximately 0.025 s can be seen in the plot shown in Fig. 3.8 using the front-right rotor as the input part, which represents approximately two rotor revolutions. The fluctuations happen more often than the previous two cases, however, this is also to be expected. The period of the fluctuations occurs approximately every 0.0031 s, which corresponds to roughly 90° of rotation at 3° per timestep. Having twice the number of adjacent rotors means that the thrust is still fluctuating every time the blade tips pass by one another. The fluctuations vary every 0.0031 s, but a trend can be observed when looking at the period highlighted by the vertical blue lines. This period covers approximately 0.0062 s or $\sim$180°, and can be seen repeated in the other three 180° periods. It seems that the change in thrust for the selected rotor varies between the two different tip interactions occurring every 90°, but the change in thrust is consistent between the same tip interaction occurring every 180°.

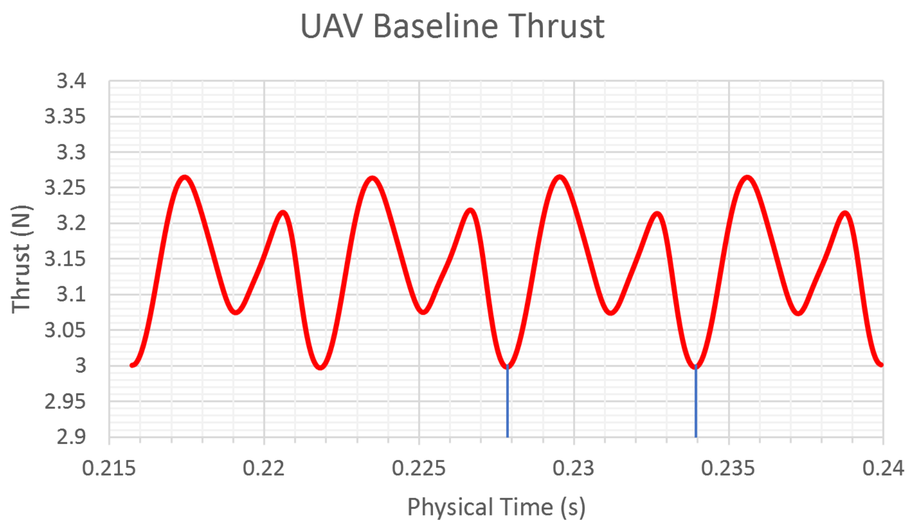

Figure 4.1: Thrust over ~0.025 s showing approximately 2 revolutions for UAV Baseline rotors.

The resulting time-averaged thrust was compared to the single rotor case here as well, which can be seen in Table 4.1. The rotor monitored for the UAV baseline case produced a time-averaged thrust of 3.132 N, which gives a drop in thrust of 1.186%. This still matches well with experiments, where the thrust dropped by ~2% [15]. While these experimental findings are for a dual rotor case, they can be applied to a quadrotor case if the time-averaged thrust is independent of rotor tip separation distance.

Table 4.1: Thrust comparison to show effects of additional rotors on time-averaged thrust.

Single Rotor Thrust (N)	UAV Baseline Thrust (N)	Percent Change (%)
3.169	3.132	-1.186

The time-averaged parameters were averaged every 180° over the last 10 revolutions here as well. Fig. 4.2 shows the k-component velocity contours on a vertical slice at the center of the front two rotors. The resampled volume was not used for the following cases as the focus is extended to the wake region as well. This figure takes the negative z-direction as positive. This image shows the same initial trend as the dual rotor case, with the retreating tip vortices being attracted towards the adjacent rotor via the Coanda effect [15, 47]. However, at approximately $z/D = 0.5$, the wake regions seem to begin to separate. This is likely a result of additional interactions between the back two rotors. The UAV arms disrupt the start of the helical core seen in previous cases, but it seems to reform near $z/D = 0.2$. Near $z/D = 1.5$, the flow being convected downwards begins to become more turbulent, and at a downstream length $\sim 2.0D$, it begins to diffuse into the still air.

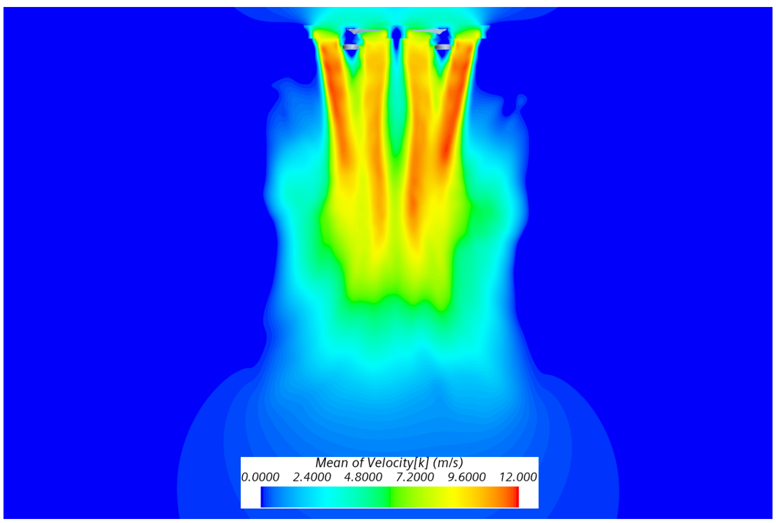

Figure 4.2: Time-averaged k-component velocity contours on a vertical slice.

Looking at the top view of the time-averaged k-component velocity contours seen in Fig. 4.3 better illuminates the cause of the phenomenon seen in the previous figure. The UAV fuselage was hidden in this image as it covers much of the area of interest. A downstream distance of $z/D = 0.4$ and $z/D = 1.5$ were used here as they were the delayed locations that best matched the separated regions found in experimental data and other published simulations[15, 30, 44]. It seems that the induced upwash from two adjacent rotors causes the wake to separate and move towards the center of the four rotors. Similar phenomena is observed but not focused on in comparable simulations for other quadrotor UAV [2, 4, 16]. This explains the phenomena seen in the previous figure, where the flow on the retreating side of the wake is pulled more towards the center of the UAV and thus away from the center plane of the rotor hub. This figure also illustrates the diffusion of the velocity that starts near $z/D = 1.5$.

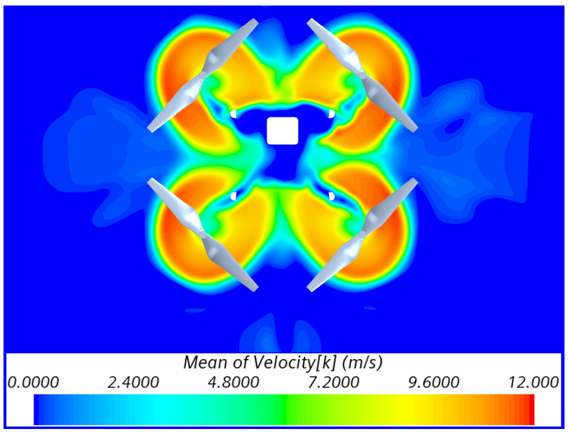

(a) $z/D = 0.4$

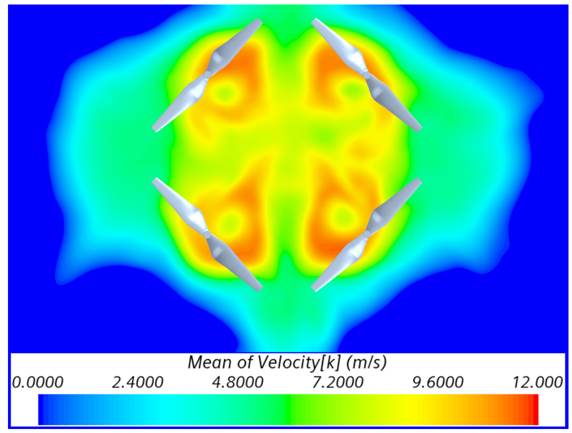

(b) $z/D = 1.5$

Figure 4.3: Time-averaged top view k-component velocity contours at (a) $z/D = 0.4$ and (b) $z/D = 1.5$.

Fig. 4.4 shows the instantaneous vorticity magnitude contours on the vertical slice. This further shows that the retreating tip vortices are being disrupted as they are pulled towards the center of the UAV fuselage, and this causes these to mix and dissipate faster than the previous cases. However, this visualizations still shows the propagation of the shear layers downstream, which occur roughly at the same distances downstream as the dual rotor case. This also better shows the interference of the UAV arms in the central vortex under the rotor hub. It seems that the vorticity actually increases as secondary tip vortices flow over the surface of the arms, seemingly causing the helical shape to be more tightly coiled as it reforms. The increase in turbulent mixing that begins at $\sim 1.5D$ downstream can also be seen better in this figure. This also shows that the wake expands to nearly double its initial size further downstream.

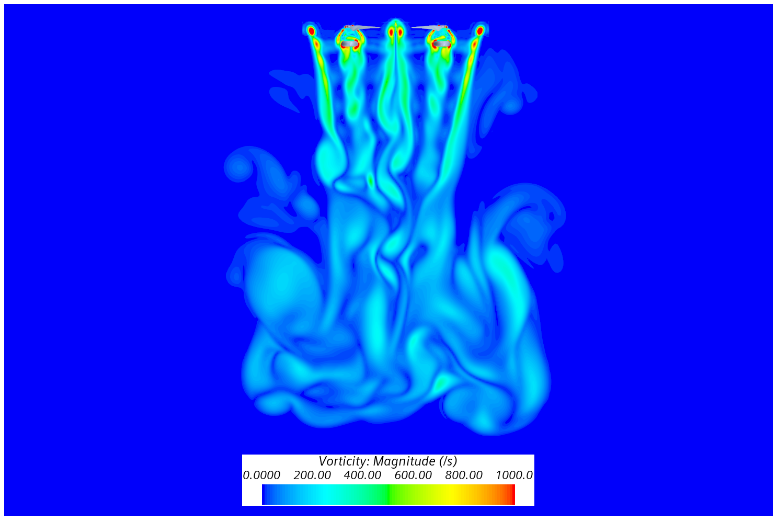

Figure 4.4: Instantaneous vorticity magnitude contours on a vertical slice.

The instantaneous i-component vorticity contours can be seen on the vertical slice in Fig. 4.5. This image shows the same general trends as the vorticity magnitude, where the retreating tip vortices are weaker at the center plane as they are pulled towards the center, and seem to dissipate faster. Once they reach $\sim 2.0D$ downstream, these vortices seem to disappear as they mix and no longer maintain their original structure. The trend seen for the advancing tip vortices is not too dissimilar from the dual rotor case and other published works [15, 44].

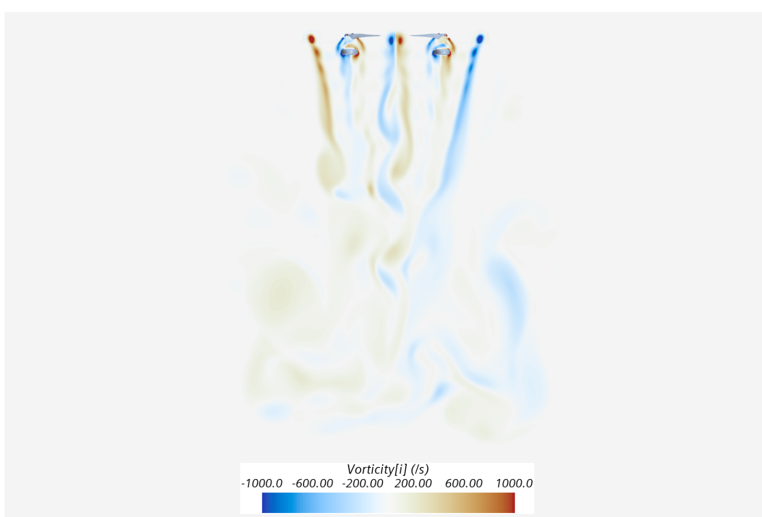

Figure 4.5: Instantaneous i-component vorticity contours on a vertical slice.

Fig. 4.6 shows the Q-criterion isosurface at a value of 20000 s^{-1} colored by the time-averaged k-component velocity contours. The positive z-direction is considered positive here. This figure better shows the phenomena of the retreating tip vortices being pulled towards the center of the UAV fuselage and away from the center plane of the rotors themselves. It also illustrates the mixing occurring within these tip vortices. The general shape of the wake is similar to what is seen in other published works [37], but with less of the smaller scales seen in higher fidelity methods. Another interesting phenomena is the turbulent region created on the top of the UAV fuselage, presumably from the convergence of the front two retreating tip vortices with the back two advancing tip vortices. Similar phenomena is seen in similar works [4, 48]. Finally, Fig. 4.7 shows the Q-criterion from a top view. This image better shows the width of the wake region as it spreads and diffuses without any ground effect. This clearly shows that the wake does nearly double in diameter by the time the vortices lose energy and diffuse into the still air.

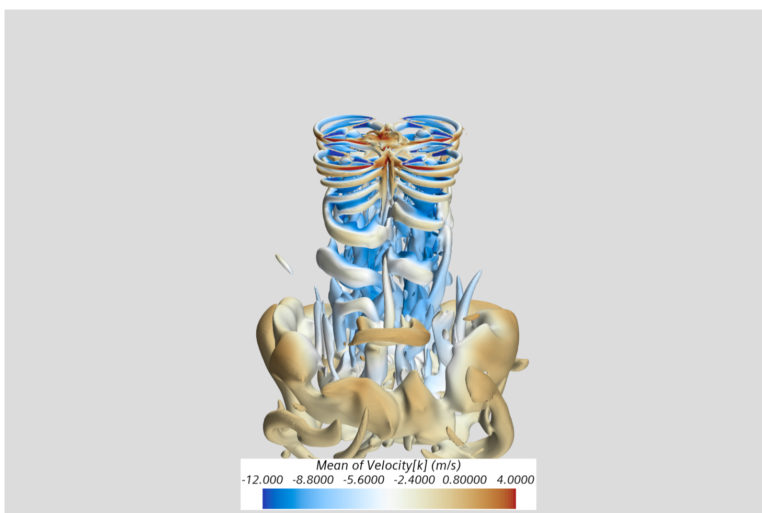

Figure 4.6: Q-criterion isosurface colored by time-averaged k-component velocity contours.

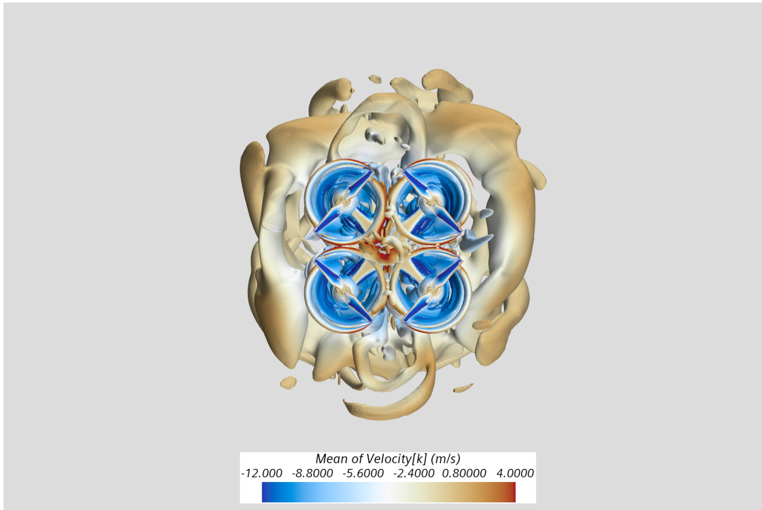

Figure 4.7: Q-criterion isosurface colored by time-averaged k-component velocity contours seen from the top.

4.2 UAV Ground Effect Cases

Ground effect plays an important role in VTOL and for near ground flight. When very close to the ground, the rotor downwash is turned which leads to an effect similar to an upwash created by the re-circulation zone that can affect rotor dynamics [11, 10]. This can also affect thrust in some cases [49]. Ground effect for rotorcraft has been investigated in many published studies [11, 10, 49, 50, 51, 52, 53, 54]. To observe these effects in the present study, the baseline case was repeated seven times simulating the UAV at ground level up to 3.0 m above ground level with a step change of 0.5 m. Ground effect was observed to be negligible beyond a height of 1.5 m when measured from the landing gear, and those cases were omitted. Normalizing the landed, 0.5 m, 1.0 m, and 1.5 m cases for the rotor's height above the ground by their diameter make them the $1D$, $3D$, $5D$, and $7D$ cases. For all cases, the same stopping criteria of 2400 timesteps and 5 inner iterations per timestep was used to have 20 full revolutions for the rotors. Looking at Fig. 4.8 shows the plots for the thrust over approximately 0.025 s showing roughly two rotations for each case when looking at the front right rotor. A period of 180° is denoted by the blue vertical lines on each plot, which is shown to contain two tip interactions that cause thrust fluctuations. While it is observed that the thrust is unaffected by ground effect by the time the UAV reaches $3D$ above ground level, there is significant change in the $1D$ case. The period of fluctuation has shifted backwards by approximately 0.0085 s, showing that the ground effect is affecting the tip interactions. The thrust peaks at a higher value, and in contrast to the other cases where the minimum thrust fluctuates between the two types of tip interactions, the minimum thrust here is more consistent. It is likely that the minimum thrust in this case is held at a more steady value based on the increase in thrust from the ground-induced upwash.

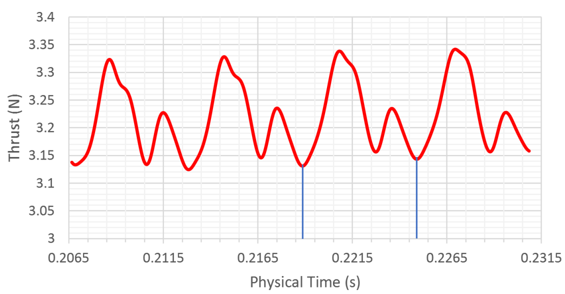

(a) $1D$ above ground

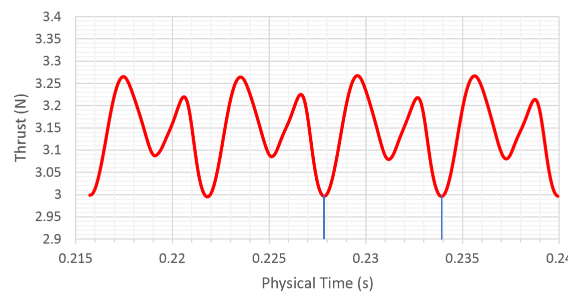

(b) $3D$ above ground

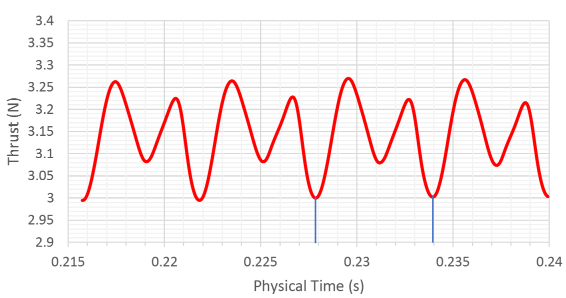

(c) $5D$ above ground

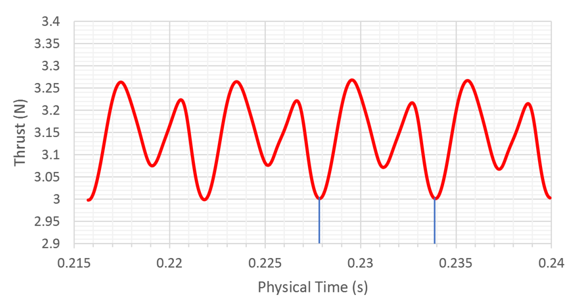

(d) $7D$ above ground

Figure 4.8: Thrust over $\sim$0.025 s showing approximately 2 revolutions for (a) $1D$ above ground, (b) $3D$ above ground, (c) $5D$ above ground, and (d) $7D$ above ground.

Table 4.2 shows the comparison of the time-averaged thrust for the near ground cases when compared against the baseline case. This shows that the time-averaged thrust is increased by nearly 3% for the $1D$ case, but is relatively unaffected once the

UAV reaches a height of $3D$ above the ground. The increase in thrust is likely a result of the additional air pushing on the bottom of the blades as the rotor downwash is redirected upward by the ground. An increase in efficiency has been observed as a result of ground-induced upwash [10], which is in agreement with the increased thrust seen here. Experimental findings show that ground effect changes the thrust the most when the rotor is below $1.0D$ above the ground, and the effect on thrust seems to become significantly lower when nearing a rotor height of $3.0D$ above the ground [49], meaning these findings are in agreement.

Table 4.2: Thrust comparison to show how ground effect changes time-averaged thrust.

Rotor Height Above Ground	Near Ground Thrust (N)	Baseline Thrust (N)	Percent Change (%)
$1D$	3.224	3.132	2.868
$3D$	3.133	3.132	0.05095
$5D$	3.135	3.132	0.1034
$7D$	3.137	3.132	0.1725

While the thrust is relatively unaffected by ground effect by the time the UAV is $3D$ above the ground, the wake reacts differently. Fig. 4.9 shows the time-averaged k-component velocity contours on a vertical slice at the center plane of the front two rotors for the four cases. This figure takes the negative z-direction to be positive. Looking at the $1D$ case, the rotor downwash is turned outwards due to ground effect, significantly increasing the width of the wake at this height. This could also be described as a result of Coanda effect [47], where the downwash is attaching to the ground and following its shape. This agrees well with what is seen in published works [11, 50, 52]. The velocity in the center of the UAV on the retreating sides of the rotor wakes is significantly lower in the $1D$ case, which is likely a result of the recirculating flow opposing the rotor downwash. This reinforces the reasoning behind the increase in time-averaged thrust seen in this case. For the $3D$ case, the wake is relatively unchanged until it reaches the point where the velocity begins to diffuse into the freestream air. The gradients here are sharper, and the wake wider, which shows the wake here is still being influenced by ground effect. Reaching a height of $5D$ shows a large reduction in ground effect on the velocity, where the wake is only slightly wider here with only the very end of the diffusing velocity interacting with the ground. At a height of $7D$ the velocity field is nearly indistinguishable from the baseline case, which shows that change velocity due to ground effect ceases entirely when the rotors are beyond $7D$ above the ground.

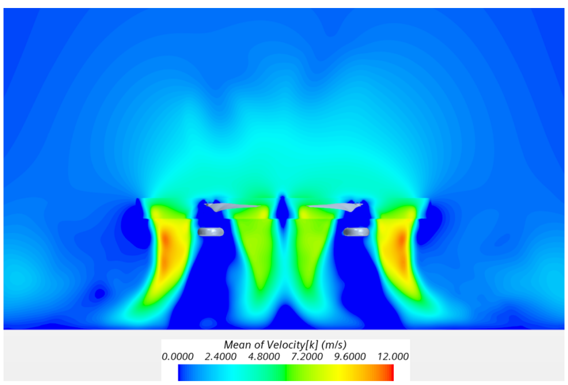

(a) $1D$ above ground

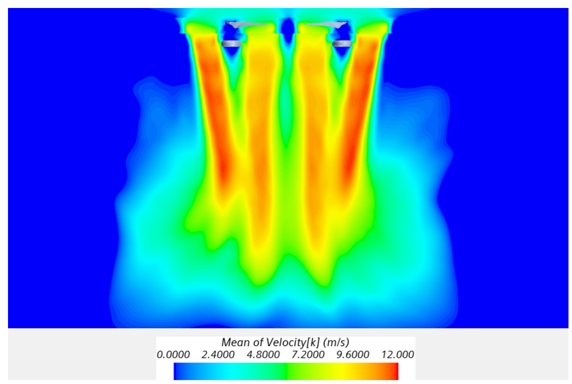

(b) $3D$ above ground

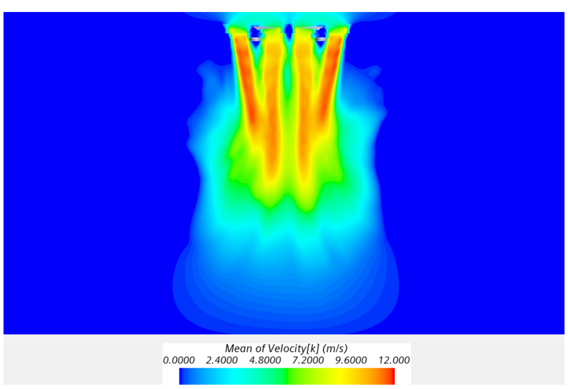

(c) $5D$ above ground

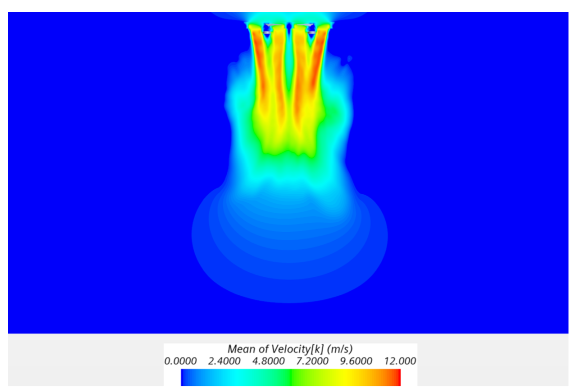

(d) $7D$ above ground

Figure 4.9: Time-averaged side view k-component velocity contours on a vertical slice for (a) $1D$ above ground, (b) $3D$ above ground, (c) $5D$ above ground, and (d) $7D$ above ground

Fig. 4.10 shows the time-average k-component velocity contours on a horizontal plane at $z/D = 0.4$. This image also takes the negative z to be positive. This shows similar phenomena to the previous figure. For the $1D$ case, the vertical velocity is significantly lower near the center of the UAV. This is also a result of the ground-induced upwash creating competing velocity as the flow is turned upwards [10]. This once again reinforces the conclusion that the increase in thrust for this case is a result of the upturned flow acting on the bottom of the rotor blades. The horizontal slices for the other 3 cases are nearly indistinguishable, which agrees with what was observed in the vertical slices, where the ground effect is only seen in the far wake region.

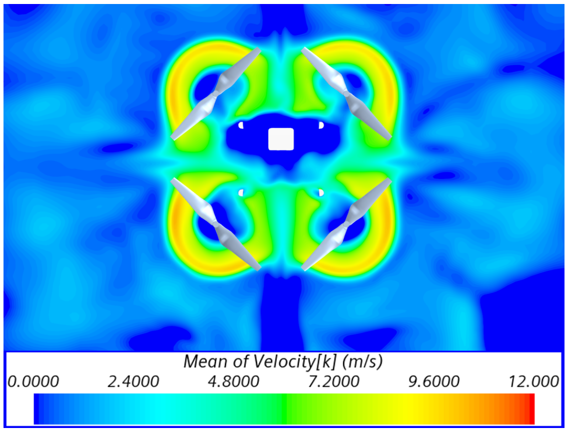

(a) $1D$ above ground

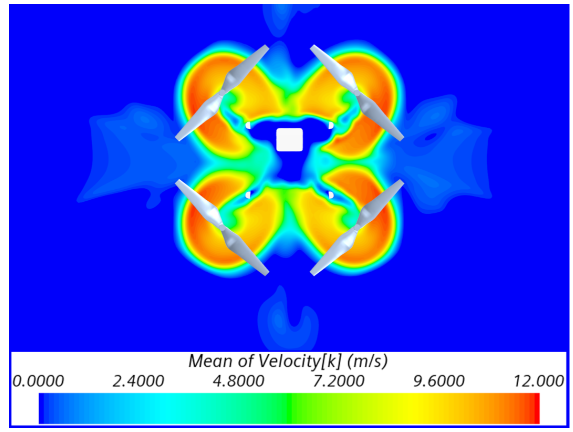

(b) $3D$ above ground

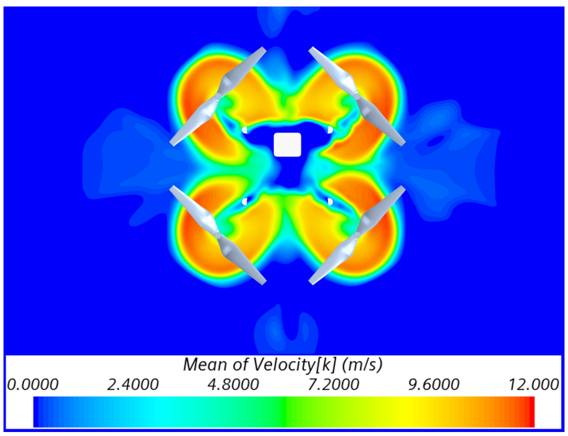

(c) $5D$ above ground

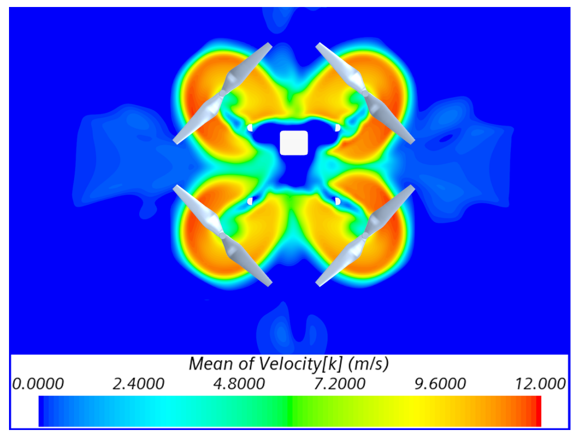

(d) $7D$ above ground

Figure 4.10: Time-averaged top view k-component velocity contours at $z/D = 0.4$ for (a) $1D$ above ground, (b) $3D$ above ground, (c) $5D$ above ground, and (d) $7D$ above ground.

Fig. 4.11 shows the time-average k-component velocity contours on a horizontal plane at $z/D = 2.0$. As this distance downstream does not exist in the $1D$ case, it is omitted here. This image takes the negative z to be positive as well. This visualization is in agreement with the vertical slices seen in Fig. 4.9, where the far wake region is wider and contains higher velocity flow in the $3D$ case as the wake is seemingly pulled towards the ground, but the other two cases show little change in the velocity field due to ground effect.

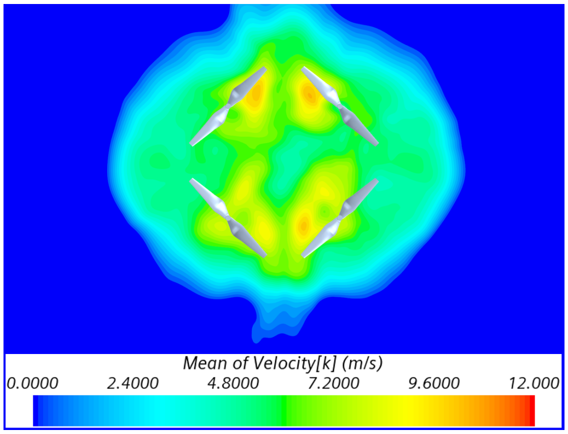

(a) $3D$ above ground

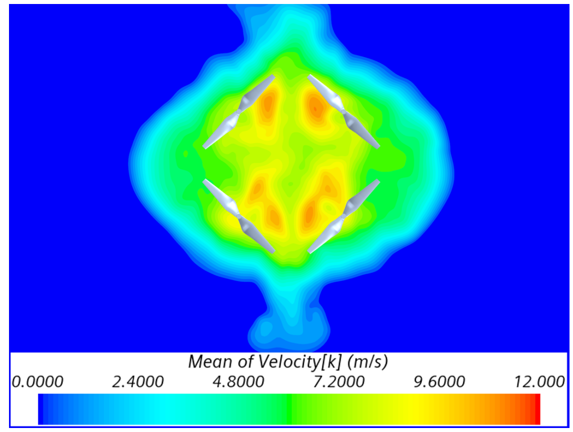

(b) $5D$ above ground

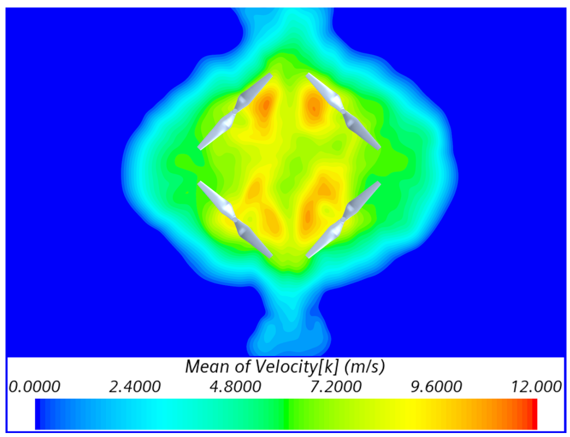

(c) $7D$ above ground

Figure 4.11: Time-averaged top view k-component velocity contours at $z/D = 1.5$ for (a) $3D$ above ground, (b) $5D$ above ground, (c) $7D$ above ground.

Fig. 4.12 shows the instantaneous vorticity magnitude contours on a vertical slice at the center plane of the rotors for the four cases. This once again shows that the wake for the $1D$ case is spread due to the ground effect, and the recirculation zones can be clearly seen under the UAV arms. The tip vortices on the retreating side of the blades are stretched downwards and dissipate almost immediately as they are caught in the re-circulating flow. This phenomena is in agreement with referenced works [11, 53]. It also shows the formation of vortices on the ground. For the $3D$ case, a large region of vorticity is created in the wake region. It seems the ground effect has a greater effect on vorticity than it does on velocity. This also shows a small region of high vorticity on the ground beneath the wake, showing that there are ground vortices forming in this case as well. The next two cases follow a similar trend as the k-velocity contours, however a bit more difference can be observed between the two. The vortices near the bottom on the $5D$ case spread further and there is even some small amount of vorticity on the ground in this case, showing that at this distance there is still some interaction of the wake with the ground. The $7D$ case again is largely the same as the baseline case, showing that the change in vorticity due to ground effect also ceases by a rotor height of $7D$.

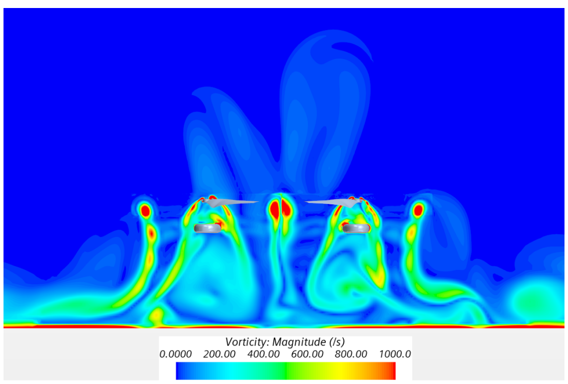

(a) $1D$ above ground

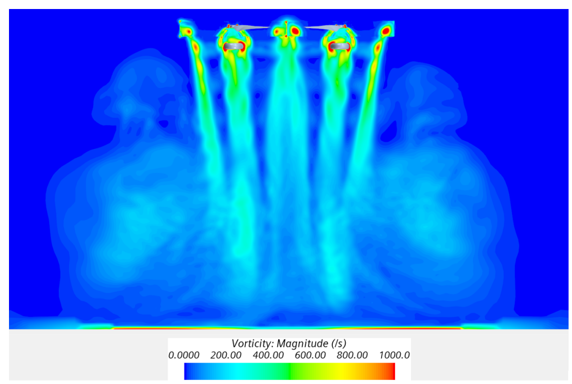

(b) $3D$ above ground

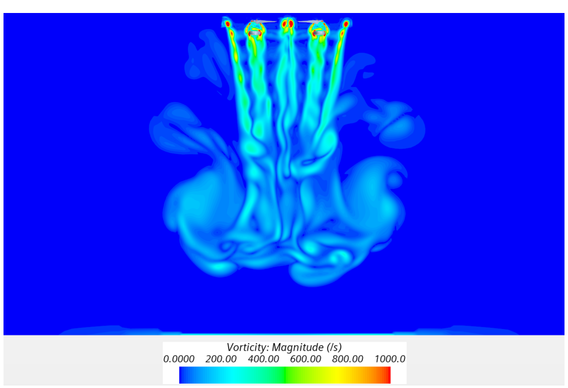

(c) $5D$ above ground

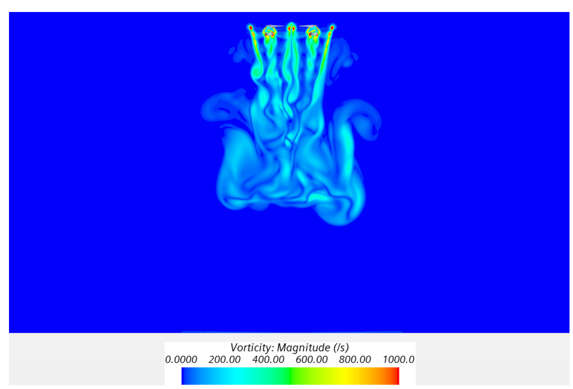

(d) $7D$ above ground

Figure 4.12: Instantaneous vorticity magnitude contours on a vertical slice for (a) $1D$ above ground, (b) $3D$ above ground, (c) $5D$ above ground, and (d) $7D$ above ground.

Fig. 4.13 shows the instantaneous i-component vorticity contours on the same vertical slice for the four cases. This figure shows that a large portion of the re-circulating flow is coming from the secondary tip vortices created by the flared portions of the rotor blades on the retreating side. This figure also shows the same effect on the retreating tip vortices as the vorticity magnitude contours. The ground vortices are also present on this visualization as well for the $1D$, $3D$, and $5D$ cases. However the in-plane vorticity on the ground for the $5D$ case is still very weak, showing that at heights any further than this and approaching $7D$ would experience little to no ground effect.

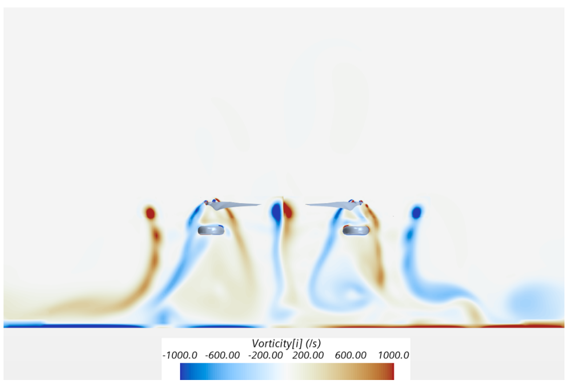

(a) $1D$ above ground

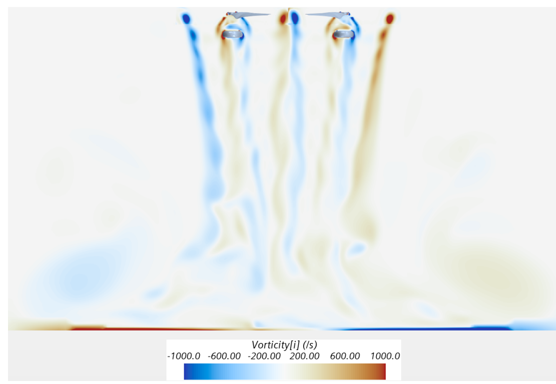

(b) $3D$ above ground

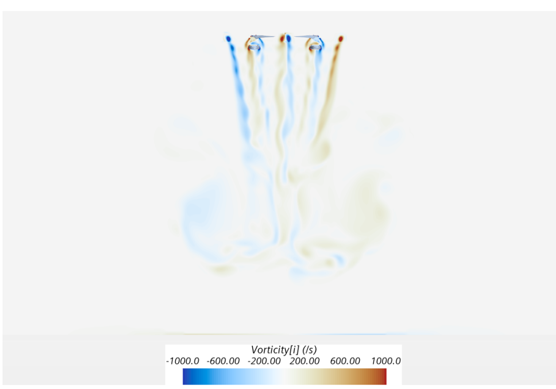

(c) $5D$ above ground

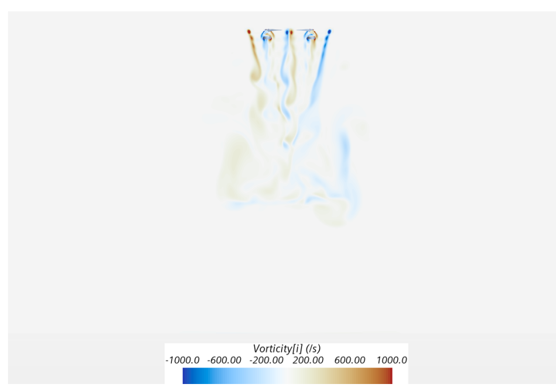

(d) $7D$ above ground

Figure 4.13: Instantaneous i-component vorticity contours on a vertical slice for (a) $1D$ above ground, (b) $3D$ above ground, (c) $5D$ above ground, and (d) $7D$ above ground.

Fig. 4.14 shows the Q-criterion isosurface with a value of 20,000 s^{-1} colored by the time-averaged k-component velocity for the four cases. The positive z is taken as positive in the Q-criterion figures. The $1D$ case here shows the tip vortices on both the retreating and advancing sides combining as they near the ground and spread to create the ground vortices, which is similarly observed in rotors in other works [53]. This also shows that the turbulent area in the top center of the UAV has increased in size and vertical velocity which is possibly a result of the effect that the induced upwash has on the tip interactions. This could be why the phase of thrust fluctuations was shifted for this case. Moving on the $3D$ case shows that the ground does indeed still have a significant effect on the wake at this height. A large circular vortex can be seen surrounding the wake at ground level. The high vertical velocity on the outside of this vortex and low velocity on the inside suggests that it was created by the combination of tip vortices as they reached the ground. The structure of Q-criterion for the $5D$ and $7D$ cases looks nearly indistinguishable from the baseline case, with the only difference being that the vortices near the bottom of the $5D$ case have slightly higher vertical velocity. This suggests that the ground is still redirecting some of the flow back upwards for this case, but the effects are only seen in the far wake region. Fig. 4.15 shows the top view of the Q-criterion isosurface to show the full width of the wake for each case. Clearly the $1D$ case shows the wake spreading the furthest, with ground vortices forming far from the UAV. However, surprisingly the $3D$ case shows the large ground vortex spreading to a width approaching the size of that of the $1D$ case. This further reinforces the conclusion that the ground effect still has a significant effect on the wake for this height above the ground. Finally, the $5D$ and $7D$ cases show the same trend as the previous view.

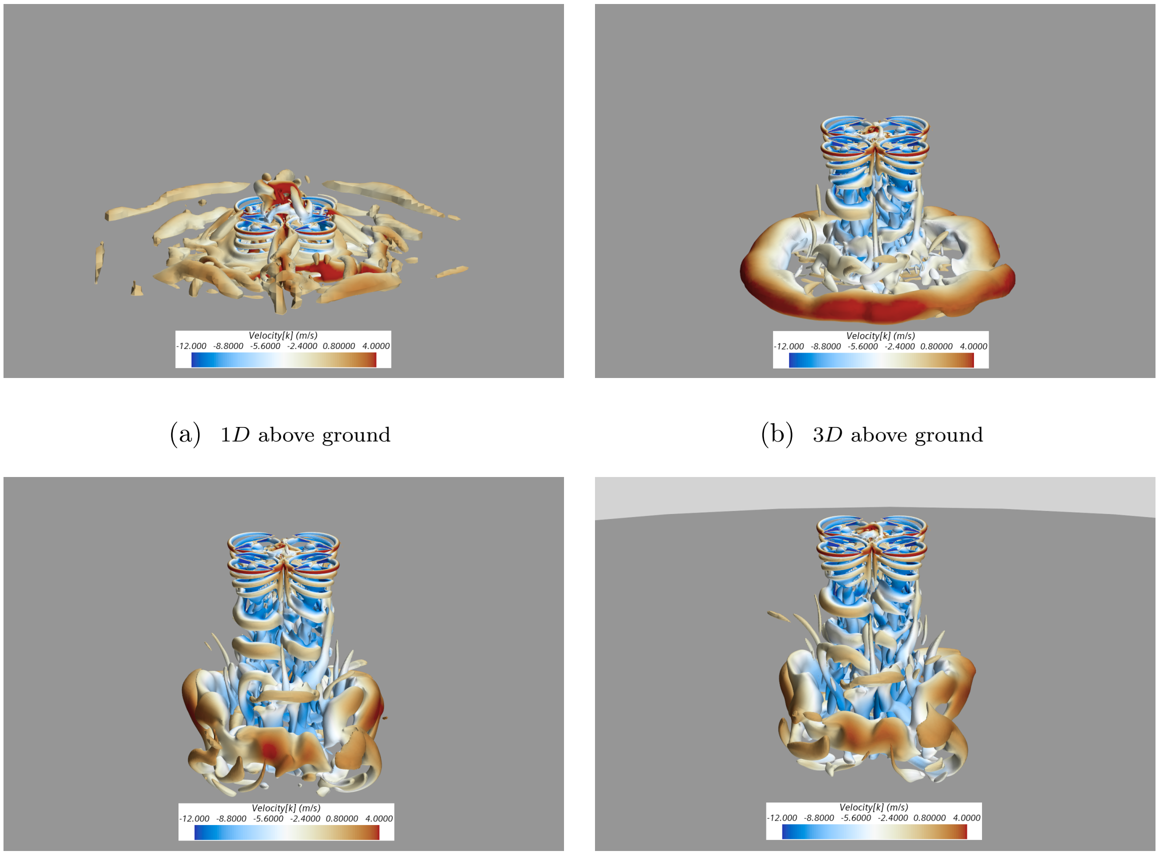

(a) $1D$ above ground

(b) $3D$ above ground

(c) $5D$ above ground

(d) $7D$ above ground

Figure 4.14: Q-Criterion isosurface colored by time-averaged k-component velocity contours for (a) $1D$ above ground, (b) $3D$ above ground, (c) $5D$ above ground, and (d) $7D$ above ground.

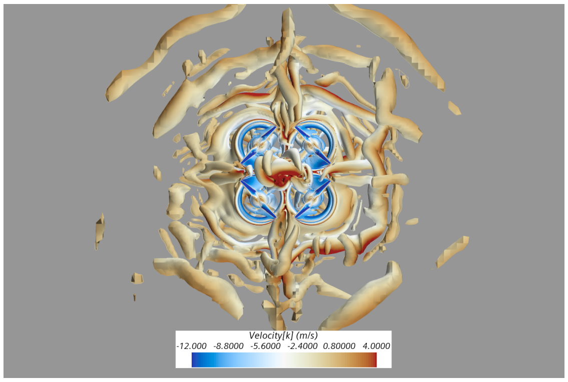

(a) $1D$ above ground

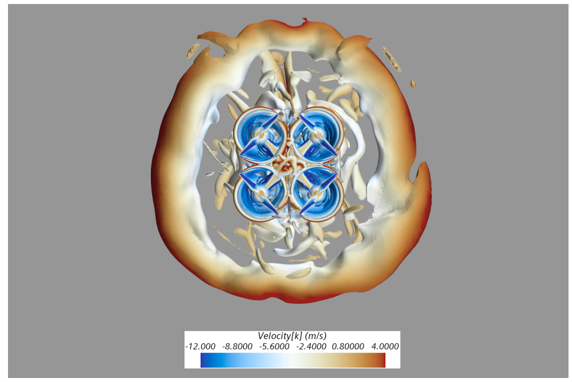

(b) $3D$ above ground

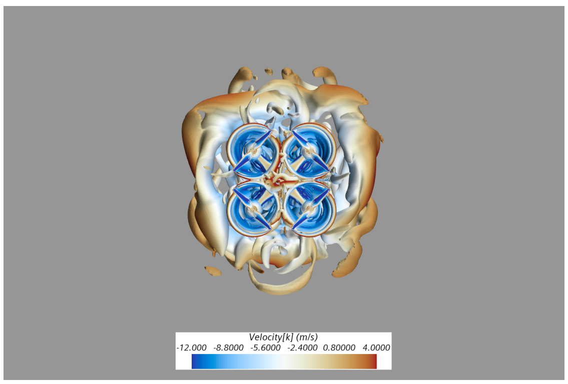

(c) $5D$ above ground

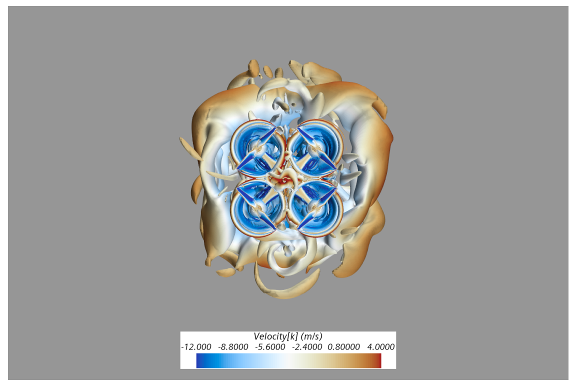

(d) $7D$ above ground

Figure 4.15: Q-Criterion isosurface colored by time-averaged k-component velocity contours seen from the top for (a) $1D$ above ground, (b) $3D$ above ground, (c) $5D$ above ground, and (d) $7D$ above ground.

4.3 UAV Dynamic Case

While ground effect can be beneficial in the form of increased thrust, it has been known to affect handling, and thus stability, negatively [11]. In the case of quadrotors it is likely a result of the increased thrust across each of the four rotors not being necessarily the same [54]. To capture this phenomena, a dynamic case having the UAV land utilizing the overset mesh was performed. For this case, the UAV was made to translate a distance of 3 m over the course of 20 rotor revolution while the pitching moment was monitored. As the vertical velocity was not considered for this case, it can be considered quasi-stationary. Fig. 4.16 shows the plot of the pitching moment over the course of the 3 m translation towards the ground. A log scale was used on the x-axis of the plot due to the large number of data points gained over the full range of time. This plot shows that the UAV begins to become unstable during descent as it enters its own rotor downwash and is subject to more unsteady flow [55]. However, this effect is significantly more pronounced once the UAV rotors reach a height $7D$ above the ground (denoted by the vertical blue line on the plot), showing that as the UAV is approaching the ground it becomes inherently more unstable due to ground effect.

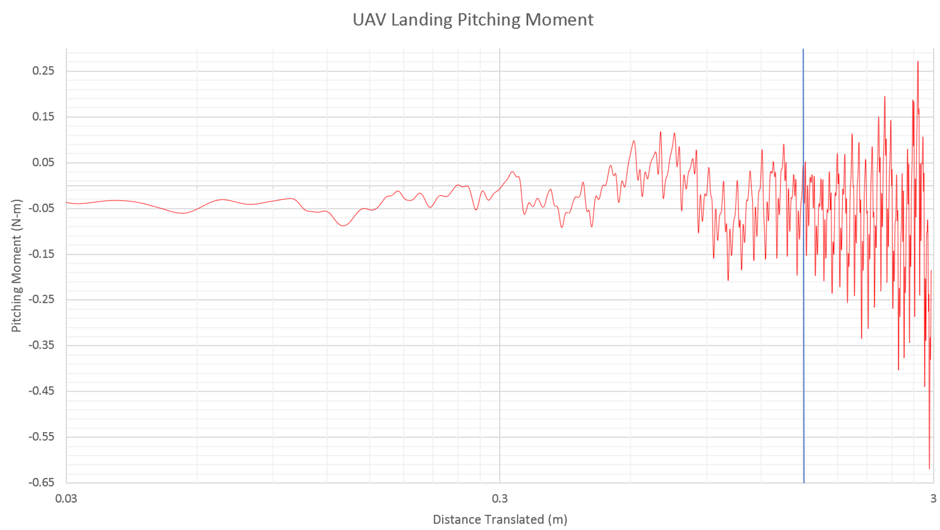

Figure 4.16: Pitching moment vs. the distance translated for the dynamic UAV case with log scale on the x-axis.

Fig. 4.17 shows the Q-criterion isosurface at a value of 20,000 s^{-1} colored by the time-averaged k-component velocity. This figure takes the positive z-direction to be positive. The Q-criterion shows that as the UAV lands, tip vortices seem projected upward as they are left behind by the descending blades. This is in agreement with studies showing rotorcraft traveling through their own downwash [55]. The separation between the tip vortices is lowered in this case, and they begin to mix and breakdown more quickly. Finally, Fig. 4.18 shows a view of the Q-criterion from below, which shows vortices beginning to shed from the landing gear and UAV fuselage. It is likely that the quicker breakdown of tips vortices observed in the previous image is a result of the interactions with these shedding vortices.

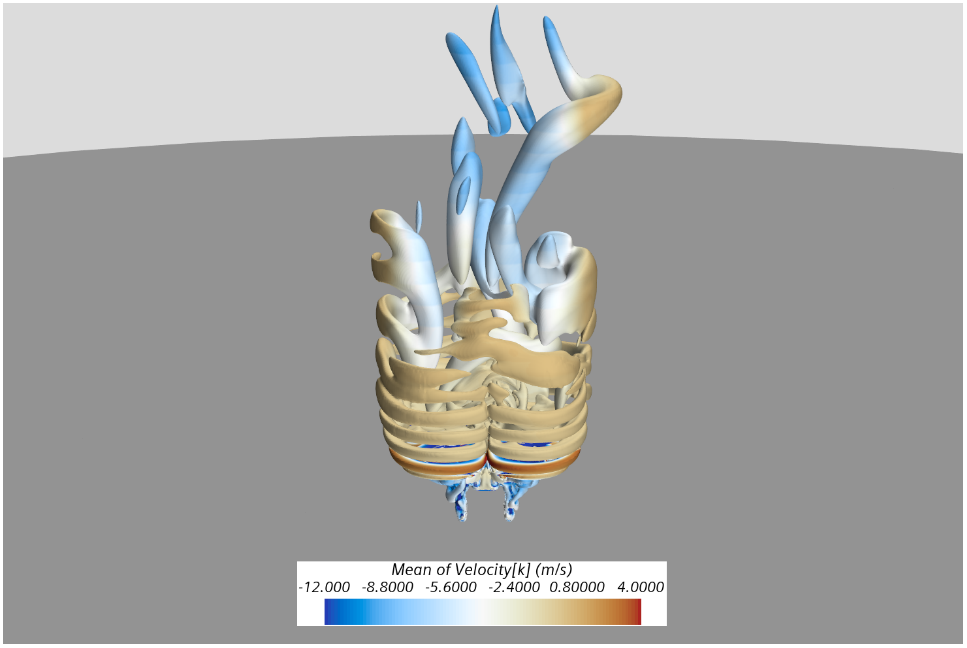

Figure 4.17: Q-Criterion isosurface colored by time-averaged k-component velocity contours.

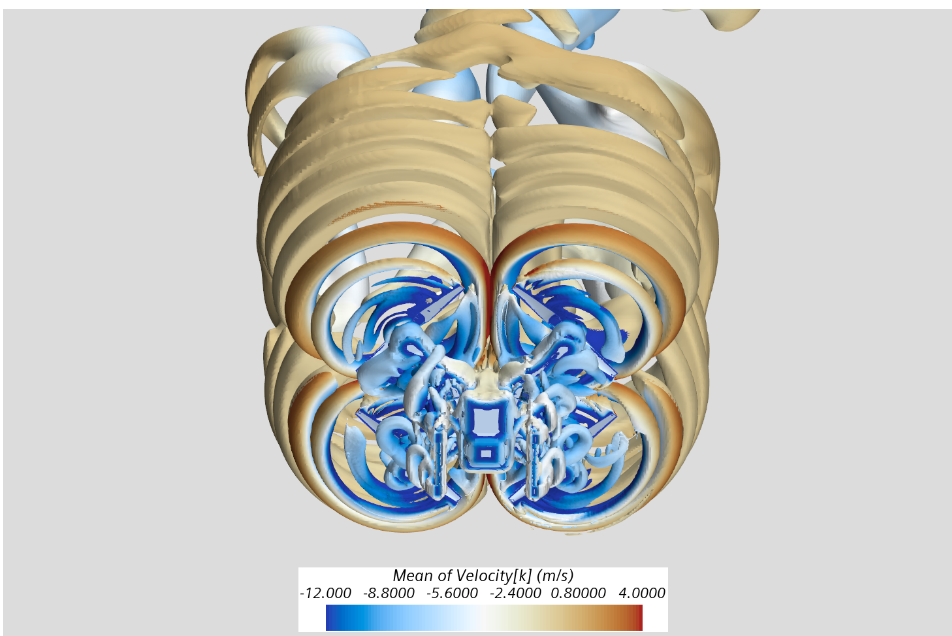

Figure 4.18: Q-Criterion isosurface colored by time-averaged k-component velocity contours zoomed to better show tip vortices.

CHAPTER 5: SUMMARY

5.1 Conclusions

The aim of the present work was to build and validate a CFD framework to investigate UAV ground effect. A combination of trimmed and polyhedral cell meshes was used in conjunction with dynamic mesh techniques like sliding and overset meshes to simulate the UAV. A single rotor was simulated as an initial case to observe accuracy of thrust predictions, which was followed by a simulation of dual rotors with a tip separation of $0.05D$ to investigate the ability to predict rotor-rotor interactions. The results showed an approximate error below 6% in the thrust, with less than 2% drop in thrust for the dual rotor case. A limitation of using a RANS method was found in the form of the delayed separated region caused by the induced upwash from rotor-rotor interactions, where the flow separation was delayed from an expected distance downstream of $0.1D$ to $0.4D$. However, this was comparable to other RANS simulations, and with the accuracy of the thrust predictions, the framework was deemed successful. A baseline UAV case was then modeled, and was compared to both the rotor interactions for the dual rotor case and the trends seen in comparable UAV simulations. Once the conclusion was made that the framework could successfully model a full UAV, several cases were run with the UAV hovering near the ground. It was determined that the thrust of the UAV was increased in the $1D$ case from the rotor downwash being reflected back towards the rotors as a ground-induced upwash. However, when at a height of $3D$ the thrust was unaffected by the ground effect. Vorticity scenes showed significant changes in the wake for the $1D$ case, where large ground vortices were created and the wake was spread much wider. This began to dissipate when reaching a height of $5D$, where the shape of the wake was significantly less affected, only showing an increase in vertical velocity from some of the flow in the far wake region being reflected upwards. Beyond a height of $7D$, ground effect was seen to be negligible. Finally, a dynamic case having the UAV translate a distance of 3.0 m towards the ground was conducted, monitoring the pitching moment to determine UAV stability in VTOL. The UAV was shown to become somewhat unstable due to traveling through its own downwash, with this instability increasing significantly when approaching $7D$ above the ground. This shows that the ground effect plays a significant role in vehicle stability.

5.2 Future Work

There are many ways that this work can be expanded upon. The first could simply be to repeat the near ground simulations with a lower step change in height. This would allow for a more accurate determination of when ground effect no longer changes the thrust. It would also be interesting to vary the phase of the rotor blades to see how rotor-rotor interactions would change. In real world scenarios, the UAV rotors may not always been in phase with one another, so varying the phase in this framework could provide insight into more real world phenomena. Another direction that could be expanded into is testing higher-fidelity methods of turbulence modeling like LES or DES. These methods tend to show less delayed separation than simpler two-equation models like k-ω. There are also plans to use the current framework to investigate the interaction between UAV rotor downwash and ground vehicle wake to gain insight on the possibility of launching UAV from moving vehicles. To lower simulation time for such complex interactions, the development of a reduced order model based upon this framework has been considered as well. Reduced order modeling would allow for a much larger breadth of studies to be performed in a more reasonable timeframe.

REFERENCES

[1] V. S. Chipade, M. Kothari, R. R. Chaudhari, *et al.*, "Systematic design methodology for development and flight testing of a variable pitch quadrotor biplane VTOL UAV for payload delivery," *Mechatronics*, vol. 55, pp. 94–114, 2018.

[2] Q. Guo, Y. Zhu, Y. Tang, C. Hou, Y. He, J. Zhuang, Y. Zheng, and S. Luo, "CFD simulation and experimental verification of the spatial and temporal distributions of the downwash airflow of a quad-rotor agricultural UAV in hover," *Computers and Electronics in Agriculture*, vol. 172, p. 105343, 2020.

[3] J. A. Mehr, E. J. Alvarez, and A. Ning, "Unsteady aerodynamic analysis of wind harvesting aircraft," in *AIAA Aviation 2020 Forum*, p. 2761, 2020.

[4] P. Ventura Diaz and S. Yoon, "Computational study of NASA's quadrotor urban air taxi concept," in *AIAA SciTech 2020 Forum*, p. 0302, 2020.

[5] B. Esakki, S. Mathiyazhagan, M. Moses, K. J. Rao, and S. Ganesan, "Development of 3D-printed floating quadrotor for collection of algae in remote water bodies," *Computers and Electronics in Agriculture*, vol. 164, p. 104891, 2019.

[6] S. Prudden, A. Fisher, M. Marino, A. Mohamed, S. Watkins, and G. Wild, "Measuring wind with small unmanned aircraft systems," *Journal of Wind Engineering and Industrial Aerodynamics*, vol. 176, pp. 197–210, 2018.

[7] R. A. Holman, K. L. Brodie, and N. J. Spore, "Surf zone characterization using a small quadcopter: Technical issues and procedures," *IEEE Transactions on Geoscience and Remote Sensing*, vol. 55, no. 4, pp. 2017–2027, 2017.

[8] D. A. Gandhi and M. Ghosal, "Novel low cost quadcopter for surveillance application," in *2018 International Conference on Inventive Research in Computing Applications (ICIRCA)*, pp. 412–414, 2018.

[9] S. Chaudhary, A. Prava, N. Nidhi, and V. Nath, "Design of all-terrain rover quadcopter for military engineering services," in *Nanoelectronics, Circuits and Communication Systems* (V. Nath and J. K. Mandal, eds.), (Singapore), pp. 507–513, Springer Singapore, 2019.

[10] H. H. Heyson, "Theoretical study of the effect of ground proximity on the induced efficiency of helicopter rotors," *NTRS - NASA Technical Reports Server*, 1977.

[11] N. Nathan and R. Green, "The flow around a model helicopter main rotor in ground effect," *Experiments in fluids*, vol. 52, no. 1, pp. 151–166, 2012.

[12] *Geometric Optimisation of Hinge-Less Deployment System for an Active Rotorblade*, vol. ASME 2011 Conference on Smart Materials, Adaptive Structures and Intelligent Systems, Volume 2 of *Smart Materials, Adaptive Structures and Intelligent Systems*, 09 2011.

[13] B. Green, *Fluid Vortices.* Fluid Mechanics and Its Applications, Springer Netherlands, 1995.

[14] M. Nitsche, “Vortex dynamics,” in *Encyclopedia of Mathematical Physics* (J.-P. FranÃ§oise, G. L. Naber, and T. S. Tsun, eds.), pp. 390–399, Oxford: Academic Press, 2006.

[15] W. Zhou, Z. Ning, H. Li, and H. Hu, “An experimental investigation on rotor-to-rotor interactions of small UAV propellers,” in *35th AIAA applied aerodynamics conference*, p. 3744, 2017.

[16] J. F. Céspedes and O. D. Lopez, “Simulation and validation of the aerodynamic performance of a quadcopter in hover condition using overset mesh,” in *AIAA Aviation 2019 Forum*, p. 2824, 2019.

[17] J. Johansen and N. N. Sørensen, “Aerofoil characteristics from 3D CFD rotor computations,” *Wind Energy: An International Journal for Progress and Applications in Wind Power Conversion Technology*, vol. 7, no. 4, pp. 283–294, 2004.

[18] O. D. Lopez, J. A. Escobar, and A. M. Pérez, “Computational study of the wake of a quadcopter propeller in hover,” in *23rd AIAA computational fluid dynamics conference*, p. 3961, 2017.

[19] O. S. Mohamed, A. A. Ibrahim, A. K. Etman, A. A. Abdelfatah, and A. M. Elbaz, “Numerical investigation of darrieus wind turbine with slotted airfoil blades,” *Energy Conversion and Management: X*, vol. 5, p. 100026, 2020.

[20] D. Su, G. Xu, S. Huang, and Y. Shi, “Numerical investigation of rotor loads of a shipborne coaxial-rotor helicopter during a vertical landing based on moving overset mesh method,” *Engineering Applications of Computational Fluid Mechanics*, vol. 13, no. 1, pp. 309–326, 2019.

[21] M. M. Yelmule and E. A. Vsj, “CFD predictions of nrel phase VI rotor experiments in NASA/AMES wind tunnel,” *International Journal of Renewable Energy Research (IJRER)*, vol. 3, no. 2, pp. 261–269, 2013.

[22] E. Yilmaz and J. Hu, “CFD study of quadcopter aerodynamics at static thrust conditions,” in *Proceedings of the ASEE Northeast 2018 Annual Conference, West Hartford, CT, USA*, pp. 27–28, 2018.

[23] F. R. Menter, M. Kuntz, and R. Langtry, “Ten years of industrial experience with the SST turbulence model,” *Turbulence, Heat and Mass Transfer*, vol. 4, no. 1, pp. 625–632, 2003.

[24] F. R. Menter, “Two-equation eddy-viscosity turbulence models for engineering applications,” *AIAA Journal*, vol. 32, no. 8, pp. 1598–1605, 1994.

[25] H. Tennekes and J. L. Lumley, *A first course in turbulence.* MIT press, 2018.

[26] J.-m. Zhan, Y.-t. Li, W.-h. O. Wai, and W.-q. Hu, “Comparison between the Q criterion and rortex in the application of an in-stream structure,” *Physics of Fluids*, vol. 31, no. 12, p. 121701, 2019.

[27] J. Hunt, A. Wray, and P. Moin, “Eddies, streams, and convergence zones in turbulent flows,” *Studying Turbulence Using Numerical Simulation Databases*, vol. -1, pp. 193–208, 11 1988.

[28] A. Schenk, “BYU flow lab schenk 2020 rotor geometries.” https://github.com/byuflowlab/schenk2020-rotor-geometries, 2020. Accessed: 2020-07-01.

[29] K. S. Madabushi, “Development of CFD simulation frameworks for high fidelity predictions of quadcopter aerodynamics,” Master’s thesis, The University of North Carolina at Charlotte, 2020.

[30] A. R. Schenk, “Computational investigation of the effects of rotor-on-rotor interactions on thrust and noise,” Master’s thesis, Brigham Young University, 2020.

[31] J. N. Abras and N. Hariharan, “Comparison of computational fluid dynamics hover predictions on the S-76 rotor,” *Journal of Aircraft*, vol. 55, no. 1, pp. 12–22, 2018.

[32] M. Misiorowski, F. Gandhi, and A. A. Oberai, “Computational study on rotor interactional effects for a quadcopter in edgewise flight,” *AIAA Journal*, vol. 57, no. 12, pp. 5309–5319, 2019.

[33] R. Steijl, G. Barakos, and K. Badcock, “A framework for CFD analysis of helicopter rotors in hover and forward flight,” *International Journal for Numerical Methods in Fluids*, vol. 51, no. 8, pp. 819–847, 2006.

[34] R. Steijl and G. Barakos, “Sliding mesh algorithm for CFD analysis of helicopter rotor–fuselage aerodynamics,” *International Journal for Numerical Methods in Fluids*, vol. 58, no. 5, pp. 527–549, 2008.

[35] J. J. Chiew and M. J. Aftosmis, “Efficient simulation of multi-rotor vehicles with low reynolds number propellers,” in *2018 Applied Aerodynamics Conference*, p. 4119, 2018.

[36] C. P. Bounds, S. Mallapragada, and M. Uddin, “Overset mesh-based computational investigations on the aerodynamics of a generic car model in proximity to a side-wall,” *SAE International Journal of Passenger Cars-Mechanical Systems*, vol. 12, no. 3, pp. 211–224, 2019.

[37] S. Thibault, D. Holman, S. Garcia, and G. Trapani, “CFD simulation of a quadrotor UAV with rotors in motion explicitly modeled using an LBM approach with adaptive refinement,” in *55th AIAA aerospace sciences meeting*, p. 0583, 2017.

[38] S. Yoon, P. V. Diaz, D. D. Boyd Jr, W. M. Chan, and C. R. Theodore, "Computational aerodynamic modeling of small quadcopter vehicles," in *American Helicopter Society (AHS) 73rd Annual Forum Fort Worth, Texas*, 2017.

[39] R. W. Deters, S. Kleinke, and M. S. Selig, "Static testing of propulsion elements for small multirotor unmanned aerial vehicles," in *35th AIAA Applied Aerodynamics Conference*, p. 3743, 2017.

[40] J. Brandt and M. Selig, "Propeller performance data at low reynolds numbers," in *49th AIAA Aerospace Sciences Meeting including the New Horizons Forum and Aerospace Exposition*, p. 1255, 2011.

[41] M. McCrink and J. W. Gregory, "Blade element momentum modeling of low-Re small UAS electric propulsion systems," in *33rd AIAA Applied Aerodynamics Conference*, p. 3296, 2015.

[42] B. Theys, G. Dimitriadis, P. Hendrick, and J. De Schutter, "Influence of propeller configuration on propulsion system efficiency of multi-rotor unmanned aerial vehicles," in *2016 international conference on unmanned aircraft systems (ICUAS)*, pp. 195–201, IEEE, 2016.

[43] D. Shukla and N. Komerath, "Low reynolds number multirotor aerodynamic wake interactions," *Experiments in Fluids*, vol. 60, no. 4, p. 77, 2019.

[44] E. J. Alvarez and A. Ning, "High-Fidelity modeling of multirotor aerodynamic interactions for aircraft design," *AIAA Journal*, vol. 58, pp. 4385–4400, Oct. 2020.

[45] E. J. Alvarez, A. Schenk, T. Critchfield, and A. Ning, "Rotor-on-rotor aeroacoustic interactions of multirotor in hover," *Journal of the American Helicopter Society*, July 2020. (in review).

[46] D. Kaya, A. T. Kutay, and O. Tekinalp, "Experimental investigation of optimal gap distance between rotors of a quadrotor UAV," in *AIAA Atmospheric Flight Mechanics Conference*, p. 3894, 2017.

[47] T. Panitz and D. T. Wasan, "Flow attachment to solid surfaces: The Coanda effect," *AIChE Journal*, vol. 18, no. 1, pp. 51–57, 1972.

[48] S. Yoon, H. C. Lee, and T. H. Pulliam, "Computational analysis of multi-rotor flows," in *54th AIAA aerospace sciences meeting*, p. 0812, 2016.

[49] P. Sanchez-Cuevas, G. Heredia, and A. Ollero, "Characterization of the aerodynamic ground effect and its influence in multirotor control," *International Journal of Aerospace Engineering*, vol. 2017, 2017.

[50] C. Paz, E. Suárez, C. Gil, and C. Baker, "CFD analysis of the aerodynamic effects on the stability of the flight of a quadcopter UAV in the proximity of walls and ground," *Journal of Wind Engineering and Industrial Aerodynamics*, vol. 206, p. 104378, 2020.

[51] D. P. Pulla, *A study of helicopter aerodynamics in ground effect.* PhD thesis, The Ohio State University, 2006.

[52] H. Otsuka, M. Kohno, and K. Nagatani, "Flow visualization of wake of a quadcopter in ground effect," in *6th Asian-Australian Rotorcraft Forum and Heli Japan 2017, ARF 2017*, 2017.

[53] B. M. Kutz, M. Keßler, and E. Krämer, "Experimental and numerical examination of a helicopter hovering in ground effect," *CEAS Aeronautical Journal*, vol. 4, no. 4, pp. 397–408, 2013.

[54] S. Aich, C. Ahuja, T. Gupta, and P. Arulmozhivarman, "Analysis of ground effect on multi-rotors," in *2014 International Conference on Electronics, Communication and Computational Engineering (ICECCE)*, pp. 236–241, 2014.

[55] M. Veismann, C. Dougherty, and M. Gharib, "Experimental studies of the rotor flow downwash on the stability of multi-rotor crafts in descent," in *APS Division of Fluid Dynamics Meeting Abstracts*, APS Meeting Abstracts, p. M18.002, Nov. 2017.